AFRL-AFOSR-UK-TR-2024-0005

Correlating manufacturing strategies to material performance in Laser Powder Bed Fusion of Titanium 6Al-4V

Tammas-Williams, Samuel
Liverpool John Moores University
Rodney House
LIVERPOOL, MERSEYSIDE, , L3 5UX
GB

12/11/2023
Final Technical Report

DISTRIBUTION A: Distribution approved for public release.

Air Force Research Laboratory
Air Force Office of Scientific Research
European Office of Aerospace Research and Development
Unit 4515 Box 14, APO AE 09421

REPORT DOCUMENTATION PAGE

PLEASE DO NOT RETURN YOUR FORM TO THE ABOVE ORGANIZATION.

1. REPORT DATE
20231211

2. REPORT TYPE
Final

3. DATES COVERED

START DATE
20190815

END DATE
20230814

4. TITLE AND SUBTITLE
Correlating manufacturing strategies to material performance in Laser Powder Bed Fusion of Titanium 6Al-4V

5a. CONTRACT NUMBER

5b. GRANT NUMBER
FA9550-19-2-7001

5c. PROGRAM ELEMENT NUMBER

5d. PROJECT NUMBER

5e. TASK NUMBER

5f. WORK UNIT NUMBER

6. AUTHOR(S)
Samuel Tammas-Williams

7. PERFORMING ORGANIZATION NAME(S) AND ADDRESS(ES)
Liverpool John Moores University
Rodney House
LIVERPOOL, MERSEYSIDE L3 5UX
GB

8. PERFORMING ORGANIZATION REPORT NUMBER

9. SPONSORING/MONITORING AGENCY NAME(S) AND ADDRESS(ES)
EOARD
UNIT 4515
APO AE 09421-4515

10. SPONSOR/MONITOR'S ACRONYM(S)
AFRL/AFOSR IOE

11. SPONSOR/MONITOR'S REPORT NUMBER(S)
AFRL-AFOSR-UK-TR-2024-0005

12. DISTRIBUTION/AVAILABILITY STATEMENT
A Distribution Unlimited: PB Public Release

13. SUPPLEMENTARY NOTES

14. ABSTRACT

An investigation into the links between manufacturing and fatigue performance for laser powder bed fusion Ti-6Al-4V has been performed. Given the reliance of the project (and much literature data) on X-ray computed tomography a study into the detection limits and repeatability of this technique was performed. Variation between users was greater than the differences reported in samples. When we tried to replicate literature results, we found that we were unable to reproduce published data. Some of this is due to inherent scatter in the process, and some due to measurement errors. We were able to demonstrate certain pore types were associated with high or low energies, and near the surface of parts. Fatigue testing of samples manufactured with a variety of melt strategies showed that we were able to manufacture samples with a better fatigue life than manufacturer recommended settings. Efforts were made to understand why some settings produced better samples than others based on the pore population. It was found that the proximity of the pore to the surface was important, and the data scatter could be reduced by using the sixth root of the pore size (µm^1/6) to normalize the stress. Artificial pores introduced into wrought and LPBF material, showed that for a given defect size, the LPBF tended to have a longer fatigue life but that life was more scattered. This suggests that we cannot fully explain the scatter in fatigue data using pore data alone.

15. SUBJECT TERMS

16. SECURITY CLASSIFICATION OF:

a. REPORT	**b. ABSTRACT**	**c. THIS PAGE**
U	U	U

17. LIMITATION OF ABSTRACT
SAR

18. NUMBER OF PAGES
65

19a. NAME OF RESPONSIBLE PERSON
DAVID SWANSON

19b. PHONE NUMBER *(Include area code)*
785-6565

Standard Form 298 (Rev.5/2020)
Prescribed by ANSI Std. Z39.18

Award number: FA9550-19-2-7001

Correlating manufacturing strategies to material performance in Laser Powder Bed Fusion of Titanium 6Al-4V

Final Performance Report

15th August 2019 - 14th August 2023

PI: Prof. Ian Jenkinson (I.D.Jenkinson@ljmu.ac.uk)

Report contributors: Dr. Samuel Tammas-Williams (s.tammaswilliams@ed.ac.uk) & Mr. Christopher Packer

Abstract

An investigation into the links between manufacturing and fatigue performance for laser powder bed fusion Ti-6Al-4V has been performed. Given the reliance of the project (and much literature data) on X-ray computed tomography a study into the detection limits and repeatability of this technique was performed. Variation between users was greater than the differences reported in samples. When we tried to replicate literature results, we found that we were unable to reproduce published data. Some of this is due to inherent scatter in the process, and some due to measurement errors. We were able to demonstrate certain pore types were associated with high or low energies, and near the surface of parts. Fatigue testing of samples manufactured with a variety of melt strategies showed that we were able to manufacture samples with a better fatigue life than manufacturer recommended settings. Efforts were made to understand why some settings produced better samples than others based on the pore population. It was found that the proximity of the pore to the surface was important, and the data scatter could be reduced by using the sixth root of the pore size ($\mu m^{1/6}$) to normalise the stress. Artificial pores introduced into wrought and LPBF material, showed that for a given defect size, the LPBF tended to have a longer fatigue life but that life was more scattered. This suggests that we cannot fully explain the scatter in fatigue data using pore data alone.

Contents

List of Figures

List of Tables

Extended Summary

A technical effort was undertaken to link the manufacturing strategy employed during laser powder bed fusion (LPBF) additive manufacture (AM) to the properties of the material produced. The project examined the link between manufacturing parameters and porosity, and porosity and fatigue life in Ti-6Al-4V components. To increase the person time available to work on this project a PhD student was funded to assist with technical aspects. This student funding has been awarded from university funds separate from the overall grant. The project was been extended by one year to make up for delays incurred due to the Covid pandemic. Fatigue testing that was originally planned to be performed in the AFRL, was instead performed at the University of Edinburgh.

Given the reliance of the project (and much literature data) on X-ray computed tomography (CT), significant work has been done to understand the uncertainty in X-ray CT measurements. Unfortunately, the results reveal significant, apparently random, error/differences between users looking at the same data. This has obvious implications when relying upon literature reported CT data to predict porosity in LPBF. In addition, when 3 data sets about 3 samples were provided to users, there was disagreement about which sample had the least porosity, which means that we cannot even assume that if published work was repeated, we would arrive at the same optimised conditions.

A statistical fit to published data has provided some insights into the links between manufacturing and porosity. However, when we attempted to recreate samples that were nominally identical to those reported in the literature, we found a different porosity to that previously reported, especially when the literature data was reported by X-ray CT. This casts further doubt on the usefulness of compiling multiple sources of data from various sources. We also found that the difference between nominally identical samples made on a single machine could be greater than the differences observed when changing laser settings.

We linked pore morphologies to energy input, with high line energy associated with approximately spherical keyhole defects. More irregular defects could be generated by using a very low hatch spacing, assumed to be due to powder denudation, or low energy, assumed to be lack of fusion.

When using manufacturer recommended settings, with small samples, we found it was possible to make small improvements (reductions) to the pore volume fraction by increasing the energy input. However, we also know that the geometry influences the number of pores so cannot be sure that this effect would be replicated across any given geometry. Furthermore, whether these small improvements are meaningful given the uncertainty outlined above remains to be seen. In addition, these small changes to the volume fraction need to be evaluated to understand whether they provide a useful change to the fatigue life of samples.

Several melt strategies were selected for manufacturing fatigue specimens, representing differing levels of porosity. For samples subjected to the same post build heat treatment, the settings defined in this project outperformed manufacturer proposed settings.

When Basquin's equation was fitted to samples made using a single melt strategy it was often able to adequately model the results. Attempts to combine data from different manufacturing strategies suggests that the pore size is less important than would be suggested by the stress intensity factor, and should be raised to $^1/_6$ rather than ½, when predicting fatigue life. The location of the pore on the other hand was a significant factor, with those at the surface associated with a shorter life. However, without more data it is difficult to draw numerical relationships.

When artificial defects were introduced into wrought and LPBF material, it corroborated our suggestion that pore size should be raised to $^1/_6$ in order to reduce the scatter in fatigue life model fitting. It was found that two defects in line with the stress behaved very similarly to a single defect, whereas when two pores were normal to the stress behaved worse than a single defect, but were not as detrimental as a defect of twice the size. When artificial defects were introduced into LPBF material it was found that LPBF outperformed wrought material subjected to the same stress intensity factor, but also showed more scatter. This implies that some of the scatter in LPBF fatigue life cannot be explained by consideration of the pores alone, and the local microstructure must be considered as well.

Our data suggests that increasing the line energy above suggested by manufacturers leads to denser, material when manufacturing small samples. We also suggest that removing the outer 0.5 mm of material from LPBF would remove an area that was found to be more porous with a range of melt strategies. However, the exact distribution of pores should be examined, to ensure any material removal does not bring a peak in porosity to the surface.

The very limited information about heat treatment we have suggests that this can have a more significant influence on the overall fatigue life than the laser manufacturing settings.

Work is ongoing to identify the exact location in the CT data where the samples failed from. This currently is a manual process requiring alignment of SEM and CT data. The PhD student will continue work with these samples to extract more data. They will try to see if the critical characteristics of the defect that lead to failure can be identified. To increase our numerical data, stepped testing will be applied to those samples that reached runout. Once failed, we can add the pore data to our analysis. More detailed fracture surface analysis will be carried out to see if the pore morphology and local environment, i.e., other pores, can be linked to fatigue life.

The PhD student who was working on this project is currently writing their thesis and will be completing in 2024. They will also complete more desk studies of existing data to try and draw further conclusions.

The CT data regarding fatigue samples will be shared with University College Dublin, alongside information about the failure location, stress, and number of cycles to failure. Machine learning will be used to try to link the pore that caused failure to the life noted.

1. Introduction

Additive manufacturing (AM) has enabled opportunities for gas turbine engine developers to increase the design space of future systems. In other words, performance benefits in turbine engines can be realized because novel design concepts via AM can be applied to critical components. Though the possible benefits of AM have galvanized the community of turbine engine designers and manufacturers, several technical obstacles need to be overcome to make AM a viable manufacturing application [1]–[3]. In the case of small-scale propulsion, the desire to attain improved thermal efficiencies, thus improving performance, calls for novel flow path componentry with complex cooling configurations [4], [5], [5]–[7]. AM applications can help small engines achieve these goals. However, structural integrity of materials associated with AM processes need to be demonstrated with minimal uncertainty. Currently, there is significant uncertainty when deploying AM metal components [8], [9], and as such they are used conservatively limiting their application. The pervasive nature of fatigue must be highly scrutinized and understood for AM generated components [10].

The aim of this project was to address these concerns by using advanced 3D material imaging techniques to characterise samples and link manufacturing strategy to defect population, and finally to fatigue test results. It focuses on the most common metal AM type [11], powder bed fusion (PBF) using a laser as the heat source (LPBF). This report includes some of the key results of the project. Results are currently being written up for publication, which will provide additional details about experimental aspects and the opportunity for our hypothesis to be scrutinised via peer review.

1.1 Project Tasks

Over the entire project the following tasks have been undertaken. Given the links between many of these tasks, they are grouped together in the remainder of the report. However, section headings are used to indicate which task they correspond to.

TASK1. Design and manufacture of a suitable object to confirm detection limits of X-ray CT system and comparison of 2D and 3D measurements
TASK2. Generate a statistical experimental design using data available in the literature and Minitab software with the aim of understanding the effect of selected process parameters on overall defect density in Ti-64 manufactured by LPBF.
TASK3. Experimental manufacture using parameters defined in the design of experiments (DoE).
TASK4. Quantify the overall defect volume fractions and relationship with process parameters.
TASK5. Employ X-ray CT to analyze selected samples and correlate individual defect types to melt strategies employed.
TASK6. Down-select melt strategy (or strategies) for manufacturing blanks for mechanical testing.
TASK7. Manufacture of blanks for fatigue testing.
TASK8. X-ray CT analysis of selected as-machined fatigue samples prior to testing.
TASK9. Fatigue testing - conducted at US AFRL.
TASK10. Identify critical characteristics of defects that lead to failure.
TASK11. Partners author a manuscript covering the results of the project for submission to the international literature.
TASK12. Suggest how to change LPBF manufacturing strategies to increase fatigue life of LPBF Ti-6Al-4V with respect to the presence of porosity.

1.2 Project Administration

The project was granted a 1 year no-cost extension to account for delays encountered during the Covid pandemic.

This project was a collaborative effort using equipment based in Liverpool John Moores University (LJMU), the Universities of Edinburgh, Huddersfield and Sheffield. Initially it was planned to use equipment at the AFRL, however, this plan was changed following discussions with AFRL, see below.

To provide additional person time to this project, a PhD studentship was provided by a separate fund (i.e., not the grant allocation).

During the project, the original PI of the project moved employment from LJMU to the University of Edinburgh (UoE). By agreement with the then monitoring officer, Shad Reed, the PI position was replaced by Prof. Ian Jenkinson, and some experimental work was subcontracted to UoE. Shad Reed has since left his position. In addition, Dr. Onome Scott-Emuakpor, due to deliver some of the project left the employment of the AFRL.

As result of these changes, a choice was made to conduct more of the experimental work at UoE, and no experimental fatigue data was collected at AFRL. Instead, fatigue testing (TASK9 on proposal) was carried out using recent investment in fatigue testing facilities at UoE.

1.3 Papers associated with this project

- Y Chahid et al., "Development of a modular system to provide confidence in porosity analysis of additively manufactured components using X-ray computed tomography," Measurement Science and Technology, Under review.
    - Reviewer comments received and revised manuscript submitted. Using results from Task 1
- F Leonard et al. "Porosity tracking throughout the laser powder bed fusion manufacturing process", Tomography of Materials and Structures, in-work
    - Using Task 4 and 5, and based on conference presentation to be given at iCT2024.
- Packer et al. "Uncertainty in CT data quantification and implications for AM optimisation", in-work
    - Currently being written by PhD student, covering results from Task 1
- Packer et al. "Inherent scatter in the mechanical properties of LPBF parts", in-work
    - Currently being written by PhD student, summarising fatigue results

1.4 Collaboration enabled

Results from the project have led to a new collaboration between UoE and University College Dublin (UCD). UCD will use machine learning techniques on the CT data collected in this project to see if the fatigue life can be better linked to porosity.

1.5 Follow-on awards or research milestones enabled by this grant

Award number FA8655-22-1-7129, from European Office of Aerospace Research and Development was awarded during this grant, using the connections established by this grant.

The University of Edinburgh has purchased a Laser PBF system, where the business case was influenced by the award of previous grants including this one. The intention is to set up a new manufacturing research institute, and again this grant is included in the business case for this.

The University of Edinburgh has invested in fatigue testing equipment and training to allow it to test metal components, as well as improve the knowledge in the materials testing laboratory personnel. The manufacturing workshop personnel have increased their skill set with regards to preparing samples with a high surface finish in a consistent manner.

A PhD student has worked on this project and has used the data to conduct their research. They are currently writing up their work for a final exam and graduation in 2024.

1.6 Teaching impact

The project aims and results have been used in undergraduate and postgraduate teaching to highlight some of the challenges when implementing metal AM into production. In addition, several student projects have been conducted:

- 5 undergraduate dissertations (from 2019-2023) completed using data or aims from this project.
- 1 PhD student, currently writing up thesis for submission in 2023– Title TBD
- MSc Thesis, Graduated 2023, Categorising Ti-Al6-4V defects in Laser Powder Bed Fusion Additive Manufacturing using Machine Learning technologies

2. Methods, Assumptions and Procedures

2.1 Quantification of detection limits of X-ray CT (TASK 1)

An artefact was designed and manufactured to test the resolution limits of X-ray CT systems. A brief description is given here, but for a full description of the manufacture, the reader is directed to the Year 1 and 2 reports [12], [13]. The artefact designed for this study was manufactured as a two-part assembly (Figure 1), which allowed area measurements acquired using 2D microscopy of the exposed surface to be compared to internal measurement using CT.

The artefact was manufactured from Ti-6Al-4V wrought stock, which was assumed to be free of any internal porosity. Following machining, the two surfaces in contact, shown by (i) and (ii) in Figure 1, were ground and polished to a 1 µm finish using standard metallurgical preparation techniques. The intention was to ensure minimal deviation (gap) between surfaces when fastened together. The two halves are near identical, apart from a M2 screw thread shown in Figure 1b. These threads will allow the two pieces to be fastened together to create a cylindrical object with similar diameter to the gauge diameter of the fatigue specimens used for mechanical testing. As such, we can assume that the absorption of X-rays would be similar for this artefact and mechanical test pieces.

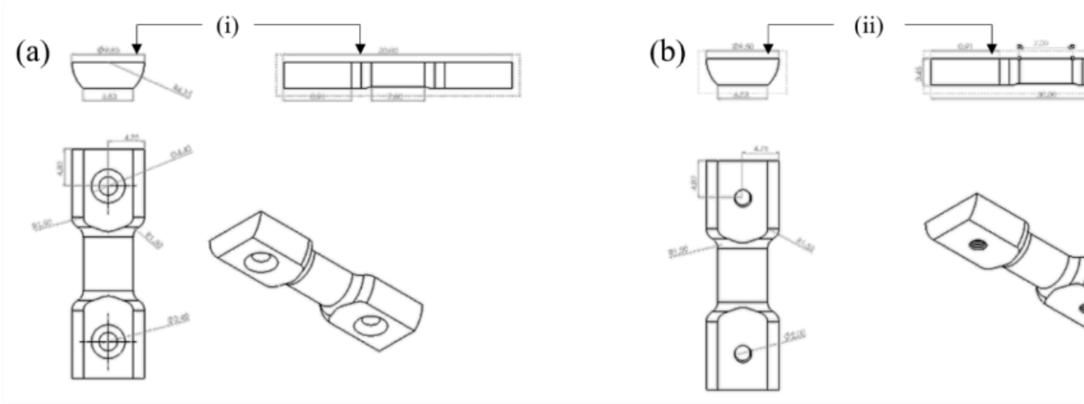

Figure 1: Two halves of sample designed to test the resolution of various inspection methods. Threaded holes allow fastening shown in (a), laser process surface marked by (ii) in (b). All dimensions given in mm.

In order to generate small internal defects, the sample was disassembled, and small holes/dimples introduced to the previously internal flat surface indicated by (i) in Figure 1a. An SPI G3 Pulsed Fibre Laser system was used to ablate material.

Preliminary experiments using rolled Ti-6Al-4V sheet were used to determine suitable settings (Table 1). The area of effect of the pulses is proportional to the natural logarithm of the pulse energy, so higher energies were used to generate larger diameter holes. The number of pulses was chosen to try and produce a dimple with equal width and depth.

Table 1: Pulse settings used to generate dimples

Width (µm)	Depth (µm)	Pulse Number	Pulse Energy (µJ)
10	10	500	120
20	20	500	160
40	40	25	300
75	75	25	640
100	100	30	800

Five sets of dimples were etched onto the sample surface, as shown in Figure 2. Each set consisting of five rows and ten columns of holes, with the intended size of the dimple at each point randomised and shown in Table 2. After laser processing, the surface was re-polished via subsequent diamond paste (6um, 3um, 1um and 1/4um) to remove the recast (crest) around the dimples.

Table 2: Intended size (µm) and position of laser drilled dimples

Row\column	**1**	**2**	**3**	**4**	**5**	**6**	**7**	**8**	**9**	**10**
1	20	10	100	20	75	75	100	10	100	40
2	100	100	20	75	10	40	75	10	75	40
3	10	40	10	20	20	20	40	75	20	20
4	100	10	75	10	75	20	10	40	75	100
5	100	10	40	20	40	100	100	40	75	40

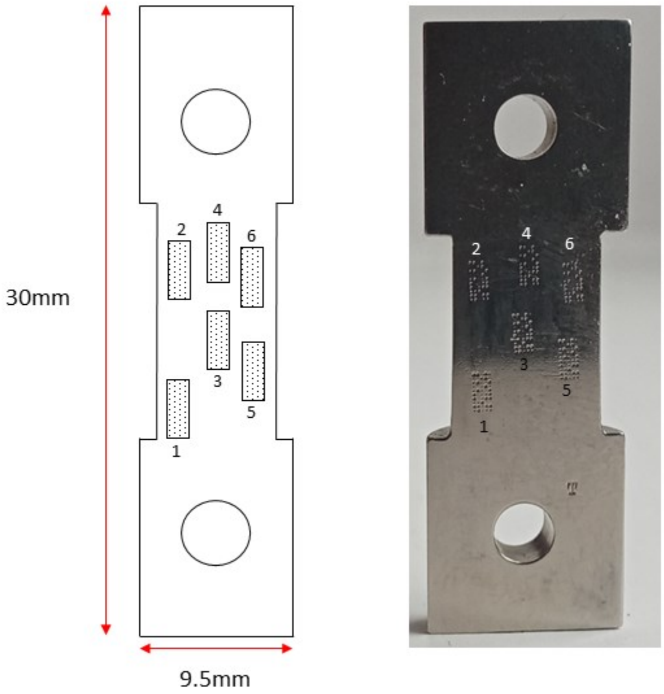

Figure 2: Disassembled artefact showing laser drilled features.

The exposed dimples diameter was measured by SEM, but it was not possible to measure the depth of the dimples. In order to estimate the effect of magnification on the detection limit the artefact was CT scanned at 3 resolutions. Specifically, with a 6 µm, 9 µm and 16 µm voxel size. The effect of various segmentation processes was then tested. All CT scanning was conducted using a Nikon XTH225.

The resulting CT volume data was sent to users at the Universities of Edinburgh, Huddersfield, Liverpool, Manchester and Warwick, and the UK Astronomy Technology Centre. This allows us to estimate the effect of user experience and the deviation in measurements when the same data is given to numerous users. A range of techniques and image processing software packages were used. Numerical data was collated to allow direct comparison between individual voids measured by CT and SEM. More details about the exact experimental set up are available in the Year 3 annual report.

The development of an improved artefact to better capture the effect of cross-sectional variation encountered in real components was also developed. This modular system required a small section of the component to be drilled, the resulting hole was then refilled by cylinder consisting of two halves with internal drilled holes, like Figure 2. For this process, micro drill bits, 120, 90, and 30 µm in diameter, were used to produce holes. More details and the full results are available in the Year 3 annual report [14], and a paper currently under review.

Finally, the influence of user data processing when analysing CT data regarding LPBF components was tested. This was done by supplying the same CT volume to all researchers and asking them to segment and quantify using their current best practice. CT regarding a Renishaw sample produced with a 30 µm layer thickness and the suggested energy input, as well as a lower and higher energy input were used. The exact experimental conditions are shown in bold in Appendix A.

2.2 Correlating manufacturing strategies to defect population (TASKS 2-5)

Meta Analysis of published literature

Published literature was interrogated to extract numerical data regarding the links between LPBF build strategies and porosity volume fraction. Where graphical information was presented, best endeavours were made to extract numerical data. Due to the different techniques used to gather and report results, there were differences in the resolution of the data. For example, some defect population was reported at 0 %, which is highly unlikely, rather it is likely that there was not a good enough resolution used by the study authors to identify the small pores. To help understand the limitations of each literature result, the method used to determine the porosity volume fraction was recorded, e.g., Archimedes, X-ray CT or optical microscopy.

A total of 240 data points were extracted. In many cases, literature data was missing key parameters. Occasionally, it was possible to back-calculate the missing data given what was presented. For example, Gong et al. [15] did not report hatch spacing, but did report the overall energy density. Some missing values could therefore be inferred by rearrangement of the equations for energy density (1) or line energy (2). Other factors, such as beam diameter, were frequently not included in published experimental records and cannot be calculated from data presented.

$$E = \frac{q}{v \cdot h \cdot l} \qquad (1)$$

$$L_e = \frac{q}{v} \qquad (2)$$

where q, v, h and l are laser power, laser speed, scan/hatch spacing and layer thickness respectively.

Numerical data was imported into Minitab software to fit a model to extract any overall trends in the data. The predictor terms selected for this model were beam power, scan speed, scan spacing, and layer thickness. Full details regarding the fitting are available elsewhere [12]. In brief, Minitab was used to fit a model to the data with a stepwise regression procedure, whereby terms are added or removed from the model based on their association with the response, in this case the porosity volume fraction. Both linear and quadratic terms as well as interaction terms were available for the model to use.

Sample manufacturing

The effect of manufacturing strategy on defect population for two different LPBF systems and processes was investigated. One was a continuous wave system, conducted using an Aconity Mini LPBF system. The other process used a modulated, quasi-pulsed laser, using a Renishaw system.

Pre-alloyed Ti-6Al-4V powder was used. The particle size distribution (PSD) was quantified using a Malvern MasterSizer, and found to have an approximately lognormal distribution as shown in Figure 3. This is typical of LPBF feedstock [16].

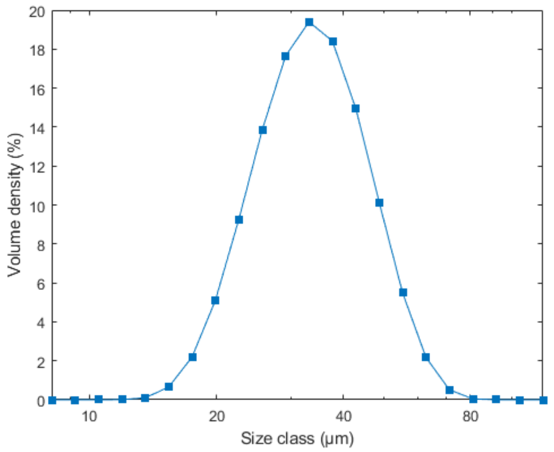

Figure 3: PSD of Ti-6Al-4V powder used to manufacture initial experimental samples. Note log scale on x-axis

Samples were manufactured with the Aconity system based on the results of the meta-analysis of literature data. Following identification of a suitable test region, a 2 factor definitive screening design was used to generate an experimental design. This allows the quality of the model to be investigated, as well as quantity the effect of manufacturing on defect population.

Additional samples were manufactured using laser settings suggested by a LPBF system manufacturer (EOS), with increases and decreases in energy input. This will allow us to test whether the EOS settings, which are developed for a different LPBF model, are useful on the Aconity LPBF system. The full laser settings are provided later alongside the measured porosity.

Finally, investigation of the literature was used to identify laser settings that were reported, alongside a volume fraction porosity. Samples were then manufactured to be identical, and to see how repeatable literature data is.

During the project, when nationwide lockdowns resulted in experimental work being paused, data from samples manufactured prior to this project, but never analysed, was used. This allowed work to continue during the nationwide lockdowns. Samples from a Renishaw AM250 at UoS were analysed. Once experimental work was possible, these were complemented by additional samples manufactured using a Renishaw AM125 at the University of Liverpool (UoL).

The quasi-pulsed nature of Renishaw sample means that rather than a speed, a distance between points (*d*) and exposure time per point (*t*) are defined. This is exemplified schematically in Figure 4 while the equations for line energy and energy density must be modified as below, equations (3) and (4). This is the process used by Renishaw AM systems.

$$E = \frac{q \cdot t}{d \cdot h \cdot l} \qquad (3)$$

$$L_e = \frac{q \cdot t}{d} \qquad (4)$$

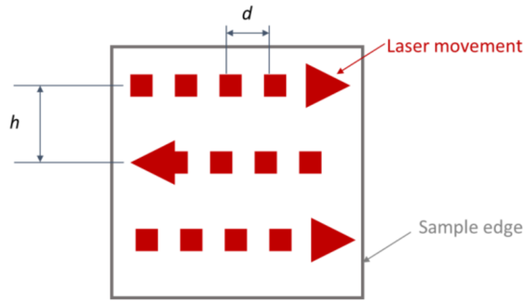

Figure 4: Schematic demonstrating the melt process used by Renishaw LPBF systems

Samples were manufactured with recommended settings for Ti-6Al-4V for both a 30 µm and 60 µm layer thicknesses. Table 3 gives the settings used for the hatching melt strategy that makes up most of the build volume. In both cases hatching was conducted using a meander strategy with a 67° rotation between each layer. Samples were manufactured as 10 mm by 10 mm by 20 mm cuboids on the AM250 using the 60 µm settings, and 6.5 mm diameter by 20 mm height cylinders on the AM125 using the 30 µm settings.

Table 3: Renishaw recommended melt strategy for Ti-6Al-4V for two different layer thicknesses

Parameters	**Values**	
Layer thickness (µm)	30	60
Power (W)	200	200
Exposure time (µs)	50	70
Point distance (µm)	75	60
Hatch spacing (µm)	65	95
Laser spot diameter (µm)	75	75
Line energy (J/mm)	0.13	0.23
Energy density (J.mm^{-3})	68	41

Modifications to the hatching melt strategy were applied to investigate how the porosity fraction was influenced. For the 30 µm layer thickness, the exposure time, point distance and hatch spacing were all modified by ±20 %. Combining all possible sets of parameters resulted in $3^3 = 27$ samples. Three additional samples were manufactured to examine the effect of changing hatching to in single direction, the order of the hatching and contouring switched, and the number of contours doubled. See appendix A for full details. All samples were analysed using low resolution CT, and three were subjected to more detailed high-resolution CT (see Appendix A).

For the 60 µm layer thickness, the exposure time and hatch spacing were varied individually. Hatch spacing's were set at 38, 60, 75 µm and exposure times at 89 and 111 µs. These values were chosen such that the same overall energy density was achieved while using different melt strategies.

X-ray CT

A range of X-ray CT systems were used during the project. Different systems were used to achieve different resolutions but also to make use of facilities during Covid lockdowns. However, whenever data is being directly compared, it will be collected on a single system. In all cases operator experience was used to choose acerating voltages and currents to provide the best signal to noise ratio.

Samples for porosity quantification were scanned in the as-built condition, i.e., prior to any stress relief. Data was segmented into solid and void using the method presented in the previous annual report and shown diagrammatically in the appendix B using Avizo software. A non-local means filter, described fully in ref. [17], and commonly recommended for processing CT data [18] was found to reduce a significant portion of the noise in the data while preserving the edges.

Effect of post build treatments on porosity

It was noted that some studies analysed samples in the as built condition, and some following a stress relief heat treatment. In addition, the heat treatments applied were not uniform. It is therefore possible that some of the scatter in the porosity data was due to pore volume changes brought about during heat treatment.

To quantify any variation in recorded porosity due to the post build stress relief treatment applied, a section of sample was cut from a block manufactured using standard Renishaw settings. This was then subjected to high resolution CT using a Zeiss Versa 520 achieving a voxel size of 1.2 µm. Following this, the sample was stress relieved, again using the Renishaw suggested strategy, 4 hours at 850 °C followed by furnace cooling to room temperature. The sample was then rescanned to quantify any changes to the porosity.

2.3 Fatigue testing and identification of critical defect characteristics (TASKS 6-10)

Sample manufacture

Four sets of laser parameters were used to generate samples using the Aconity Mini LPBF system. These were chosen to represent varying levels of porosity (Table 2). A and B were based on the meta-analysis of literature data, whereas Aconity and EOS were based on settings suggested by the named manufacturer.

Table 4: Settings used to manufacture samples with continuous wave laser for fatigue testing

Setting group	***A***	***B***	***Aconity***	***EOS***
Power (W)	190	190	200	170
Scan Speed (mm/s)	550	317	1200	1250
Scan Spacing (mm)	0.145	0.12	0.8	0.1
Layer Thickness (mm)	0.03	0.03	0.03	0.136
Beam Diameter (mm)	0.13	0.13	0.07	0.1
Porosity volume fraction (%)	0.80	5.90	-	<0.01

All samples were built in a vertical orientation and slightly oversized (0.5 mm) from the final test dimension (Figure 5). The addition stock was added to allow the samples to be machined smooth following AM, and avoid the influence of different surface roughness's. After manufacture they were removed from the baseplate by wire EDM.

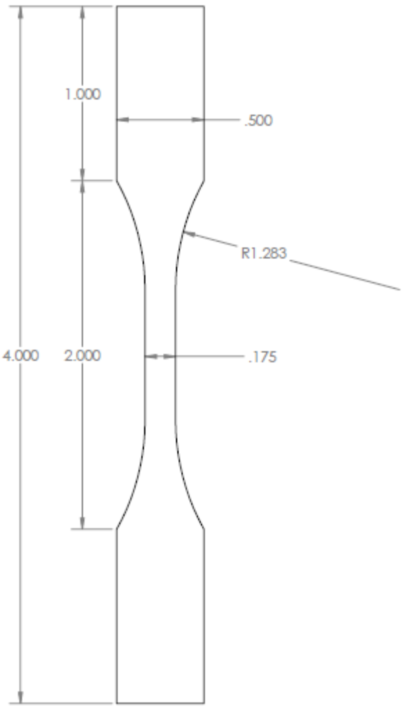

Figure 5: As-machined cylindrical geometries used for fatigue testing, dimensions in inches. Dimensions supplied by AFRL.

Samples were then subjected to a heat treatment to relieve the residual stress built up during LPBF. The heat treatment cycle was 4 hours at 650 °C in an air furnace, i.e., conforming with aerospace materials specification AMS-H-81200D [19]. The use of air is acceptable as any oxide layer/alpha case formed will be removed by the subsequent machining step. Previous modelling has suggested oxide oxygen diffusion depth of approximately 35 µm from the surface of titanium after 420 h at 650 ˚C with an unlimited supply of oxygen [20], significantly less than 0.5 mm that was subsequently removed.

Due to the time requirement for EDM, transit between sites, and finally heat treatment, there was a significant gap between sample manufacture and stress relief. This is thought to have led to cracking in some samples, but interestingly only one batch, which indicates that some laser settings result in a higher propensity to crack due to residual stress. This is discussed in section 3.3.

In addition to the continuous wave laser PBF samples, 16 samples were manufactured using Renishaw recommended parameters for 60 µm layer thickness. 8 of these were subjected to laser drilling (see below). These were subjected to a standard Renishaw heat treatment, which was 850 for 4 hours, so significantly higher than used for the other samples. Finally, 8 Renishaw samples manufactured and tested as part of a different AFRL project (award number FA8655-22-1-7129) are presented here as they allow us to quantify the effect of the heat treatment on the results, as they were subjected to the same heat treatment as the Aconity samples.

Machining of all samples was conducted using a XYZ machine tools CNC lathe, equipped with ProtoTrak SLX control software. Wrought bar of the same alloy was used to develop the process, and minimise the surface roughness after machining. All samples were examined using a Laser Scanning Spectral Confocal Microscope (Leica TCS SP2) before testing. The surface roughness recorded was typically between 0.2 and 0.6 µm, significantly smaller than the porosity under investigation.

X-ray CT

X-ray CT was conducted using the µCT system at the University of Edinburgh to identify both the overall pore volume fraction as well as individual pores that have potential to initiate cracks after the samples had been machined. The length of the specimens meant each sample consisted of 3 separate CT scans that were then aligned and merged after the data collection. The data was analysed using methods shown to produce reasonable alignment with microscopy examination in Task 1.

Generating artificial defects

To allow a more systematic analysis of the effect of defect size and proximity of others on fatigue life, laser drilling was employed to introduce small dimples into both wrought and AM material. This represented an extension of a similar approach to understand fatigue limits in wrought titanium using mechanical drilling [21].

Dimples of various size were produced. The same laser processes developed for the resolution checking object was used, as earlier work had identified good parameters for consistent dimple sizes. All were intended to have a depth approximately equal to their width. Using wrought titanium, five samples of each with 40 µm, 75 µm and 100 µm dimples were produced (total 15). In further wrought samples, holes were drilled approximately 1 of their diameters apart, to examine the impact of proximity of defects. Pairs were drilled both aligned and normal to the applied stress direction. Two of each direction and size were produced, producing 12 samples with paired defects. A total of 27 laser drilled samples were thus produced from wrought material. In addition, 4 holes of 75 µm and 4 holes of 100 µm were produced in 8 samples manufactured from Renishaw material.

By using a laser to drill these holes, to was assumed that they would better represent the natural defects that occur in AM titanium then production by another method, such as mechanical drilling demonstrated previously [21].

It was hypothesised that two holes perpendicular to the stress would behave similarly to one pore of a size equivalent to the total of the two pores' sizes. Conversely, it was hypothesised that two holes in line with the stress would act as a smaller pore, as the stress is likely to be reduced [22] by the presence of another hole.

Mechanical testing

Fatigue testing was carried out at the University of Edinburgh using an Instron 8802 servo hydraulic fatigue testing system. Instron wave matrix 2 control software was used to setup and run tests.

Conversations with AFRL revealed that there was most interest in fully reversed (R = -1) testing, which was used for all tests. Testing was carried out until the sample broke or 1 million cycles had passed.

Fractography and post build analysis

Analysis of the broken samples was conducted using SEM. Manual examination of the surface was used to identify initiation location of the critical fatigue crack.

Basquin's equation (5) was used to fit a model to the fatigue results, linking the stress amplitude (σ_a) and number of cycles to failure (N).

$$\sigma_a = \sigma_f' \cdot \left(2 \cdot N_f\right)^b \tag{5}$$

Where σ_f' is the fatigue strength coefficient, b is the fatigue strength exponent and $2N_f$ is the reversals to failure.

When fatigue cracks initiate from pores, various studies suggest that the pore area normal to the applied stress is key in determining fatigue crack initiation [9], [23], [24]. A high-resolution image of this pore was taken, and then ImageJ [25] was used to manually measure the area. The lack of contrast between the pore and the cracked surface feature precluded the use of automatic segmentation techniques. To reduce the error, 3 measurements were taken for each pore, and both sides of the broken sample were examined leading to a total of 6 measurements for each feature.

It has been reported that normalising fatigue stress data (σ_a/σ_w) by an estimated limit at 10^8 cycles reduces scatter significantly [9] for other AM types. The fatigue limit (σ_w) was estimated as equation (6).

$$\sigma_w = 1.43 \cdot \frac{HV+120}{\left(\sqrt{A_n}\right)^{1/6}} \tag{6}$$

Where HV is the Vickers hardness and A_n is the pore area normal to the stress. It was assumed the measured pore area on the fracture surface was equal to the pore area normal to the stress, but it is possible that samples cracked away from their max area, e.g. ref. [26]. It has been suggested that the exponent in equation 8 should be different for different sized defects [21]. We have not measured hardness values here but we assume the same hardness throughout. The normalised stress ($\sigma_n = \sigma_a/\sigma_w$) is therefore:

$$\sigma_n = \frac{\sigma_a}{1.43 \cdot \frac{HV+120}{\left(\sqrt{A_n}\right)^{1/6}}} = \frac{1}{1.43 \cdot (HV+120)} \cdot \sigma_a \cdot \left(\sqrt{A_n}\right)^{1/6}$$

$$\sigma_n = C \cdot \sigma_a \cdot \sqrt{A_n}^{1/6} \tag{7}$$

Where C is a material constant to account for the hardness. Throughout this report, the hardness was assumed to be 350 HV [27], which results in C = 1/672.1. Basquin's equation was then fitted again using the normalised stress.

Others have suggested that scatter can be reduced by plotting the stress intensity factor (K_I) generated by the pore at the crack initiation site, estimated using the equation proposed by Murakami [24], eq. (8).

$$K_I = 0.65 \cdot \sigma_a \cdot \sqrt{\pi \cdot \sqrt{A_n}} \tag{8}$$

Where the constant 0.65 is used to account for the pore location. For surface pores 0.65 is used, whereas for subsurface pores 0.5 is used.

Basquin's equation was also modified to use a stress intensity factor rather than stress, as per (9):

$$K_I = K_f' \cdot \left(2 \cdot N_f\right)^c \tag{9}$$

Where K_f' and c are materials constants analogous to σ_f' and b.

The similarities between equation 7 and 8 are clear, the major difference being that equation 7 takes no account of pore location, and raises the pore size to $^1/_6$ rather than $^1/_2$. We therefore create a second normalised stress, that incorporates the effect of surface using the value proposed by Murakami, i.e. 0.65 for surface pores, and 0.5 for internal pores. As a result, the second normalised stress (inc. position) used the same equation 7, but the constant C was modified as:

- C = 0.5/672.1; for subsurface pores, and
- C = 0.65/672.1; for surface pores.

Clearly, this estimate of the constant is very basic, but it does allow the effect of surface pores to be amplified. As more data is collected it may be possible to refine this value. Basquin's equation was again fitted to this second normalised stress.

Thus, 4 methods for plotting the fatigue data were tested, to examine whether any provided clues as to scatter in the data.

3. Results and Discussion

3.1 Understanding detection limits and uncertainty in X-ray CT (TASK1)

When the same data was given to different users, the number of pores detected changed. In other words, the same practical experimental set up could result in different numerical data being extracted. The detection limit was a function of both the resolution used and the user (Figure 6). At the higher resolution there was limited difference between users, but as the resolution decreased the more experienced users were better able to detect the smaller pores. However, even among the more experienced users there were differences in the number of pores detected.

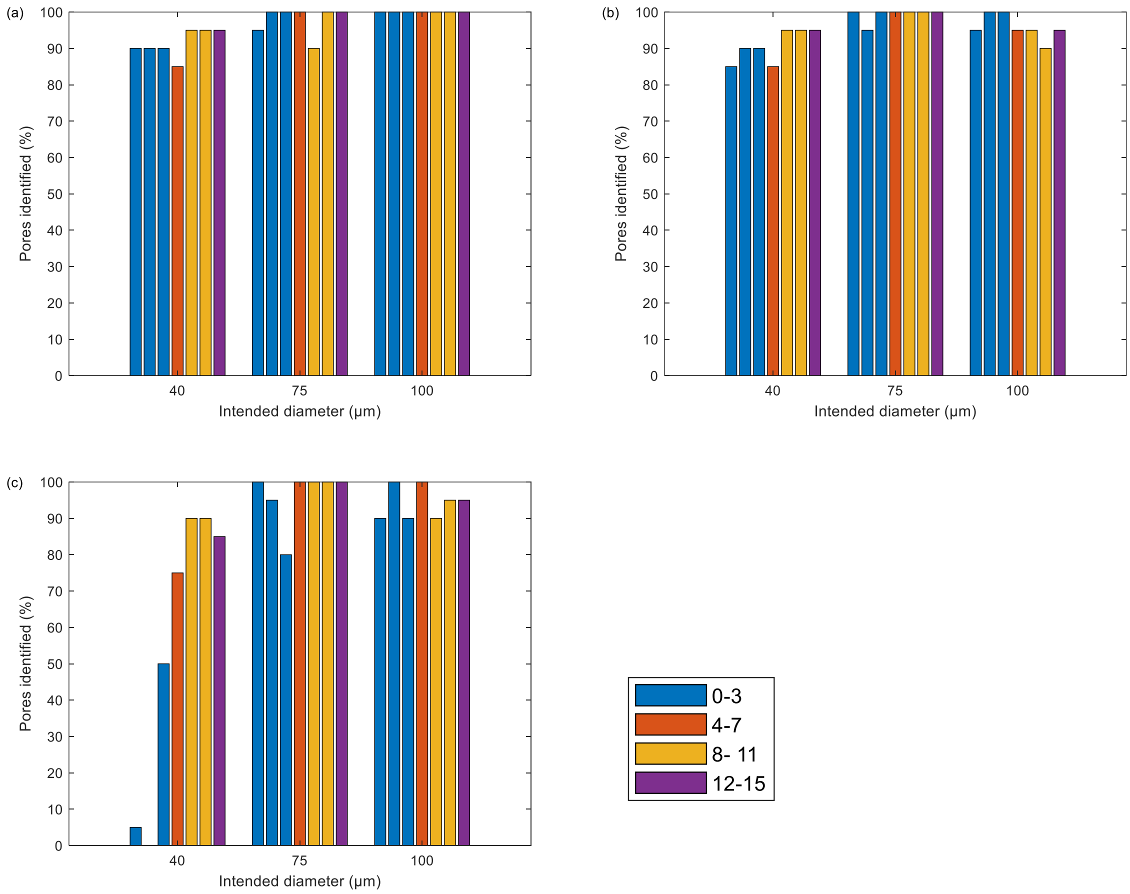

Figure 6: Percentage of artificial pores detected by different users, at 3 different resolutions, (a) 6 µm, (b) 9 µm and (c) 16 µm voxel size. The colour of the bar indicates the approximate experience in years of the user.

While Figure 6 above gives information about whether users detected porosity, it gives no information about the users' measurements of the porosity. When CT size measurements are compared to SEM measurements, Figure 7, most users measured the voids in the CT as larger than on the SEM. It should be noted that the SEM measurement comes with its own uncertainty, and as it is only measuring the exposed diameter, it is possible that the void was larger beneath the viewed surface. However, what is clear is that the same set of voids were measured as having different sizes by different users. The data for each individual pore can be viewed in the year 3 report [14].

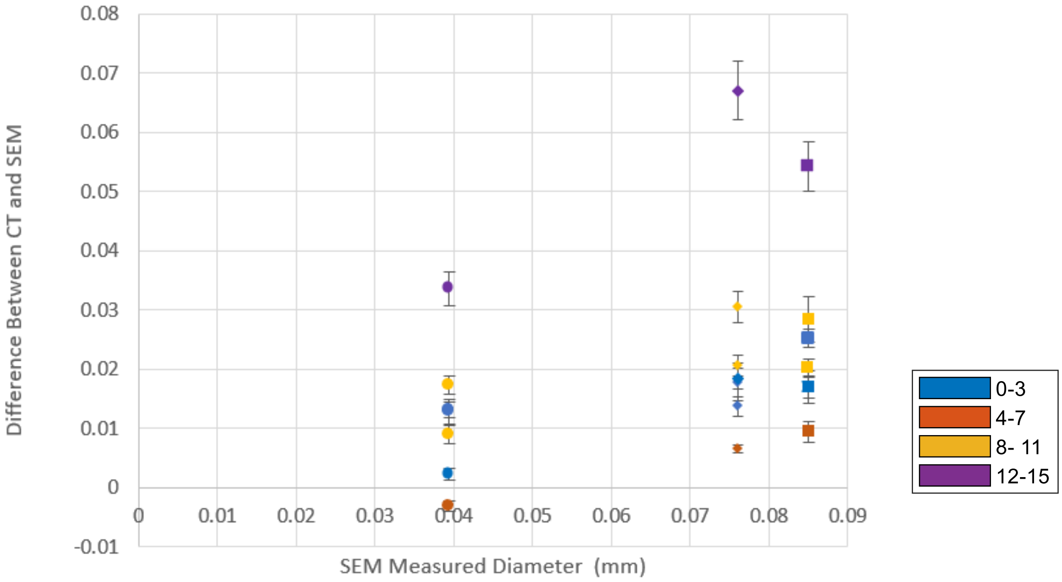

Figure 7: Mean difference between void diameters measured by SEM and CT. Error bar indicates standard deviation. Color indicates user experience in years of working with CT

When the same set of users was given CT data concerning 3 LPBF samples manufactured with different laser settings, there was also significant variation in results. The total volume fraction of porosity recorded was different for all users, in some cases, by orders of magnitude (Figure 8a). While all users agreed that the data regarding the low energy sample had the most porosity there was disagreement about the absolute volume (note the log scale).

If the users' processes were introducing a systematic error, then we may be able to detect this by normalising the volume fractions with one another, in this case, by dividing the high and low energy volume fraction with the "optimized" energy volume fraction. However, when viewed on Figure 8b, there are differences in the relative volume fractions. Perhaps most concerning was the disagreement about which sample was "best" i.e., the lowest porosity. Most users agreed the high energy sample had a lower volume fraction than the optimised energy sample, i.e., less than 1 on Figure 8b, but not all. There were also significant differences in how much less porous it was.

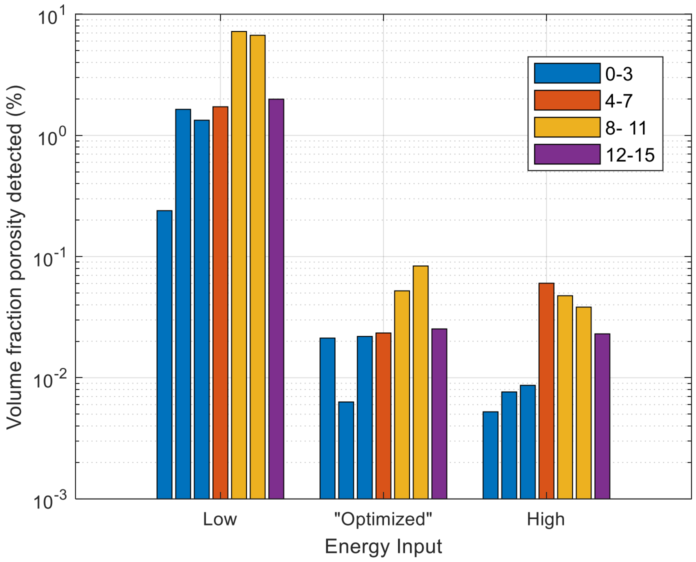

a)

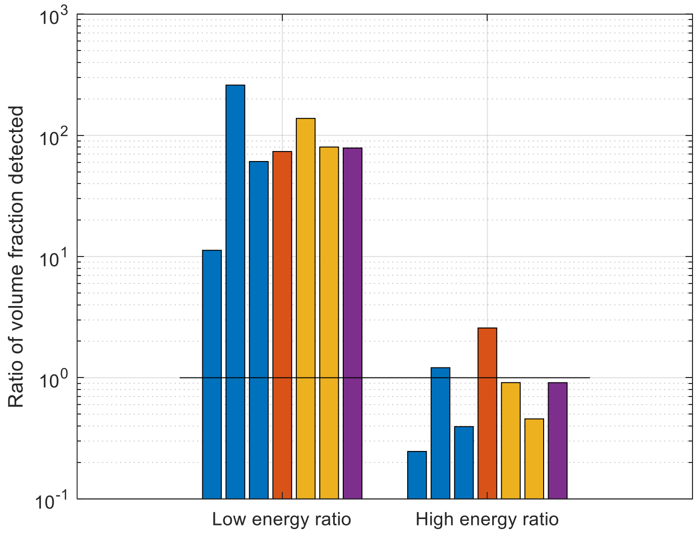

b)

Figure 8: Volume fraction porosity measured by different users of good Overall volume fraction porosity measured by different users all given the same raw data regarding three samples. Note log scale.

Given the current lack of standardisation in CT data processing it is not entirely surprising that when the same data is given to multiple users, each user reported slightly different results. This is due to differing approaches to segmenting the data. Conversations with users revealed that in many cases, the "automatic" approaches (e.g. Otsu [28], ISO50) were felt to be poor and so most users used some level of subjective judgement when defining and measuring porosity.

Taken as a whole, the results in this section are concerning, particularly as much literature that uses CT to quantify porosity gives limited information about how the data was processed. This implies that where studies have quantified the links between porosity and laser parameters via X-ray CT, we must interpret these with caution. If another user had conducted the analysis the results could have been different. This is the case even for relatively experienced users (>8 years). However, it should be noted that much academic research is done by PhD students, who (by definition) have more limited experience.

Furthermore, here we may have underestimated the issue of CT uncertainty. All users were given the same data to process, which eliminates any uncertainty around X-ray collection/reconstruction. When comparing previously published data, each study is likely to have used slightly different X-ray CT setting when gathering the data, which is likely to further compound the problem. Even if identical X-ray settings were used, each data set would have a slightly different level of noise, which may influence the data.

3.2 Linking process parameters to defects (TASKS2-5)

Meta analysis of literature data

When the individual process parameters are plotted against reported pore volume fraction (Figure 9), there is limited useful information that can be identified. While low power and high speeds resulted in the highest pore fractions recorded, they also allowed very low fractions. Similar variation is notable in the calculated values for line energies and energy densities. Perhaps the most interesting result is the minimum line energy required for a highly dense component (< 0.5 % porous) appears to be approximately 0.1 J/mm to 0.2 J/mm. This may be indicative of a minimum energy requirement in order to maintain a stable melt pool in Titanium 64. However, what is clear is that none of the terms presented in Figure 9 are suitable to predict porosity in isolation. Thus, it is necessary to plot the data in multi-dimensional space. In order to interpolate between the data available, regression analysis was used.

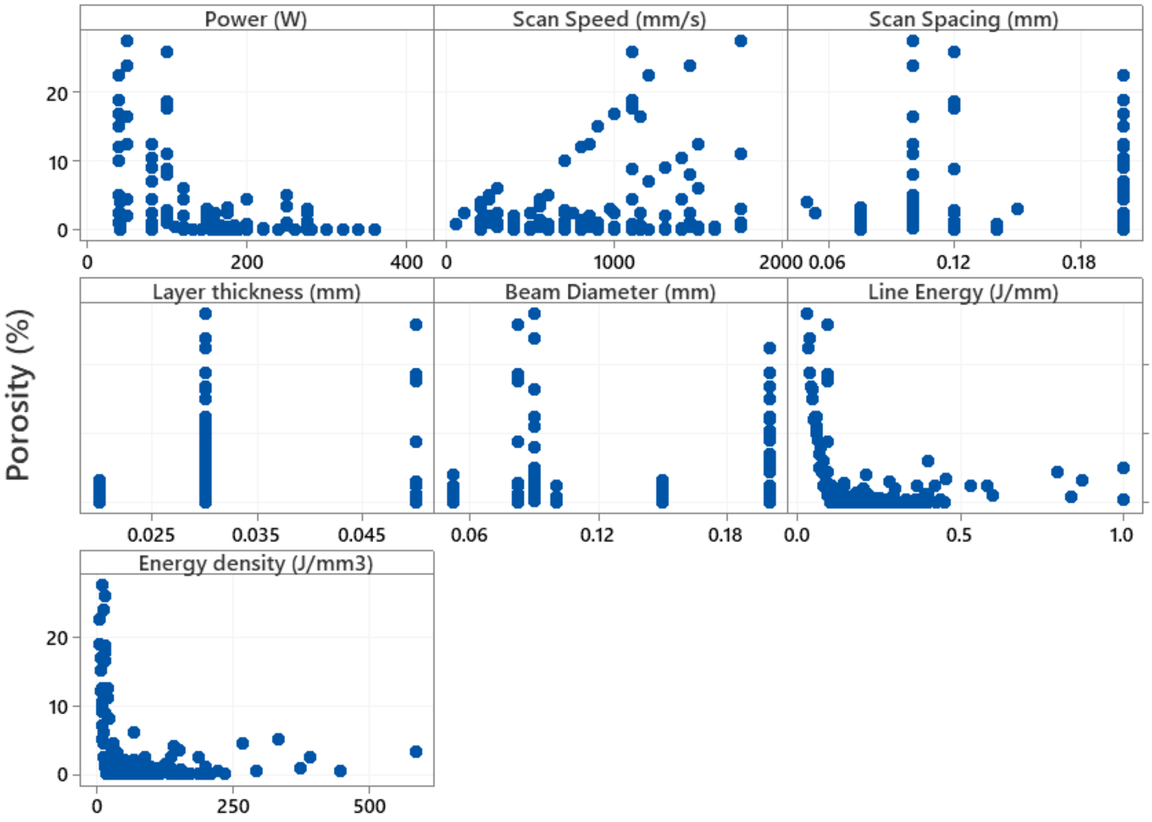

Figure 9: Porosity against individual process parameters recorded from the literature.

To generalise the empirical model and avoid using the PBF machine model as an input, the beam diameter was estimated. It was assumed that most modern PBF equipment would use a similar wavelength laser so this was not included. It was assumed that the beam radius would be approximately equal to half the hatch spacing based on previous review of the literature [29]. When a study used multiple hatch spacings, the beam radius was set to half the control/centre point hatch spacing. Hence, beam diameter was included as a numerical predictor in the refined model.

Prior to model fitting some points were culled from the data to avoid the model being influenced by unusual predictor values. The circled region indicated in Figure 10a shows an example of usual data, where the line energy calculated was orders of magnitude greater than other data. Similarly, very high speeds (Figure 10b) were excluded from the model. In either case, inclusion of these data would have greatly increased the range of the model without significantly increasing the data available. Furthermore, the experimental conditions were so radically different from other available results it suggests that either the experiment had a fundamental difference that was not recorded, or there was an error in the data collection/reporting.

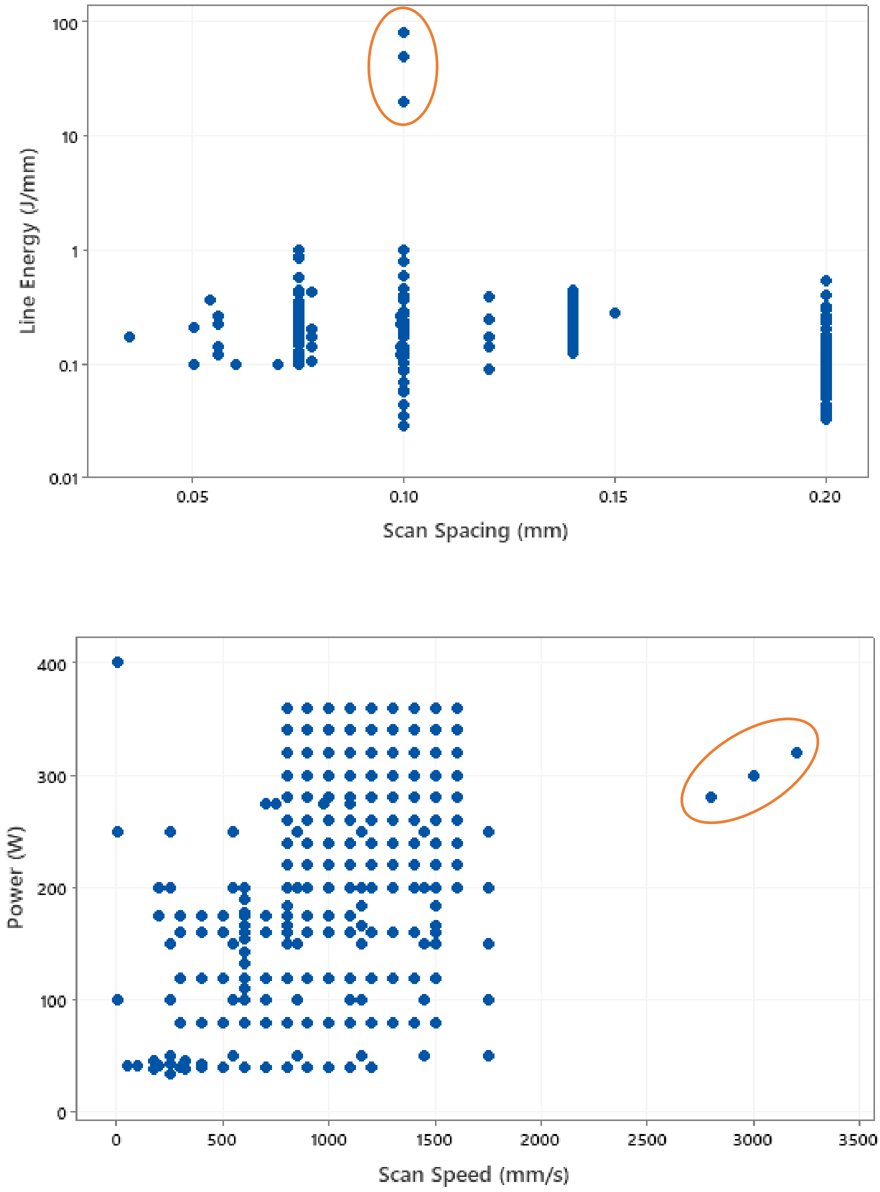

Figure 10: Experimental data from literature showing variation of predictors. Unusual data excluded from model is circled.

When a regression model was fitted using the commonly reported inputs (Figure 9) the R^2, i.e., percentage of variation explained by the model, was 79 %. The predicted R^2, where individual data rows are removed, the model refitted and then predictions made, was 75 %.

All terms that related into the energy input were found to have a statistically significant link to the porosity. However, the effect of the beam diameter was regarded as insignificant with this set of data.

This could be caused by the lack of data available and the need to estimate the beam diameter in many cases. In addition, when beam diameter was stated by a study, it was rarely varied, and instead simply a constant for the entire experiment.

Another issue with the collected data is a correlation between predictors. For example, while there is no physical reason why scan speed should be a function of other predictors, in practice, when setting up experiments higher scan speeds will often be chosen alongside higher powers, lower layer thicknesses etc. This leads to high levels of correlation between factors. This may result in issues if the model were used to predict porosity outside of the "normal" range of inputs, and the result will be less reliable. That said, the predictor ranges are generally chosen to be those thought to produce good quality samples, so in most cases this is where predictions of porosity are likely to be most useful.

To visualise the effect of process parameters on porosity, example contour plots of predicted porosity (%) have been plotted in Figure 11. When not included as a variable, a power of 190 W, scan speed of 850 mm/s, scan spacing of 0.13 mm and layer thickness of 0.03 mm were used. The blue dots show the experimental conditions examined (and discussed later).

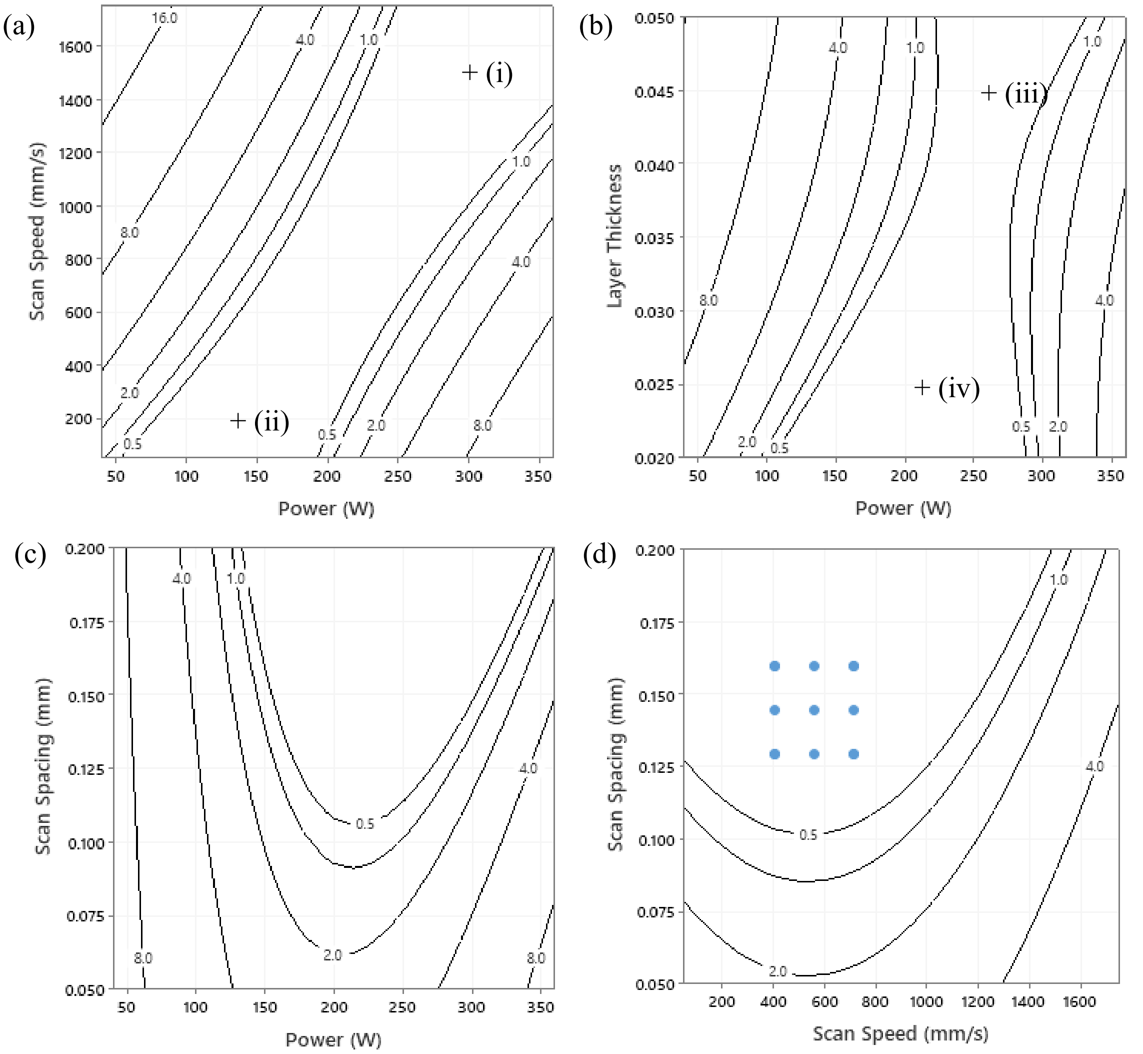

Figure 11: Contour plots of porosity model from literature data showing predicted porosity for various build settings. In (c) the first set of experimental data points is shown.

While caution should be used when interpreting these plots due to the varying sources, quality of data used and purely empirical nature of the fit, many of the calculated relationships can be rationalised by considering the physical processes they correspond to. When scan spacing and layer thickness are fixed

(Figure 11a), and reading across for a given scan speed, porosity first decreases with power, before reaching a minimum and then increasing. The first set of pores are likely to correspond to lack of fusion caused by insufficient energy input. As the power increases, larger melt pools eliminate these pores. However, further increases in power can lead to vaporisation of the material (key holing) and void generation.

As the speed increases the required power for low porosity also increases. This is expected given the reciprocal relationship between speed, and energy input, which can be quantified with line energy (J/mm) or energy density (J/mm^3) (equations 1 & 2). In other words, higher speeds require a higher power to deliver the same overall energy. However, line energy/energy density alone is not enough to explain this shift, and the low-density region does not have a consistent line energy, as may be expected based on absolute energy input alone. Two points in approximately the centre of the low porosity region are shown in Figure 11a. The line energy at point (i): q = 300 W, v = 1500 mm/s, is 0.2. J/mm, whereas at (ii): q = 140 W, v = 200 mm/s, is 0.7 J/mm. At the higher speed the required line energy is reduced to only 28 % of that at lower speeds. This apparent inconsistency in energy required to fully consolidate the powder may be explained by considering the effect of time. For a constant geometry, as speeds increase the time available for heat to dissipate between beam passes will reduce. Thus, the energy required to raise the material above its melting point is reduced, which allows a reduced line energy to be used effectively. Similar empirical relationships have recently been experimentally observed in titanium alloys [30].

A similar trend is apparent between layer thickness and power when scan spacing and speed are fixed (Figure 11b), with higher layer thicknesses needing a higher power to remain in the low porosity region. This is logical given the larger volume of material to be melted. Again, energy input is not consistent throughout the low porosity region, with energy density ranging from approximately 52 J/mm^3 at point (iii) to 76 J/mm^3 at (iv). A physical explanation for this difference is currently unclear, but is likely to be related to the amount of retained heat. This observation that thinner layers require a higher energy input can be corroborated by inspection of the recommended Renishaw parameters in Table 3, where the 30 μm layers are associated with 68 J/mm^3 and the 60 μm layers with 41 J/mm^3 energy density.

Experimental test of empirical model

Two tests were conducted with different sized samples, the first with 10 mm cubes, the second with 6.5 mm cylinders. A voxel size of 9 μm and the adaptive thresholding technique was used. A visual representation of typical slices of the CT data is given alongside the overall extracted overall volume fraction in Figure 12, which also indicates the model prediction.

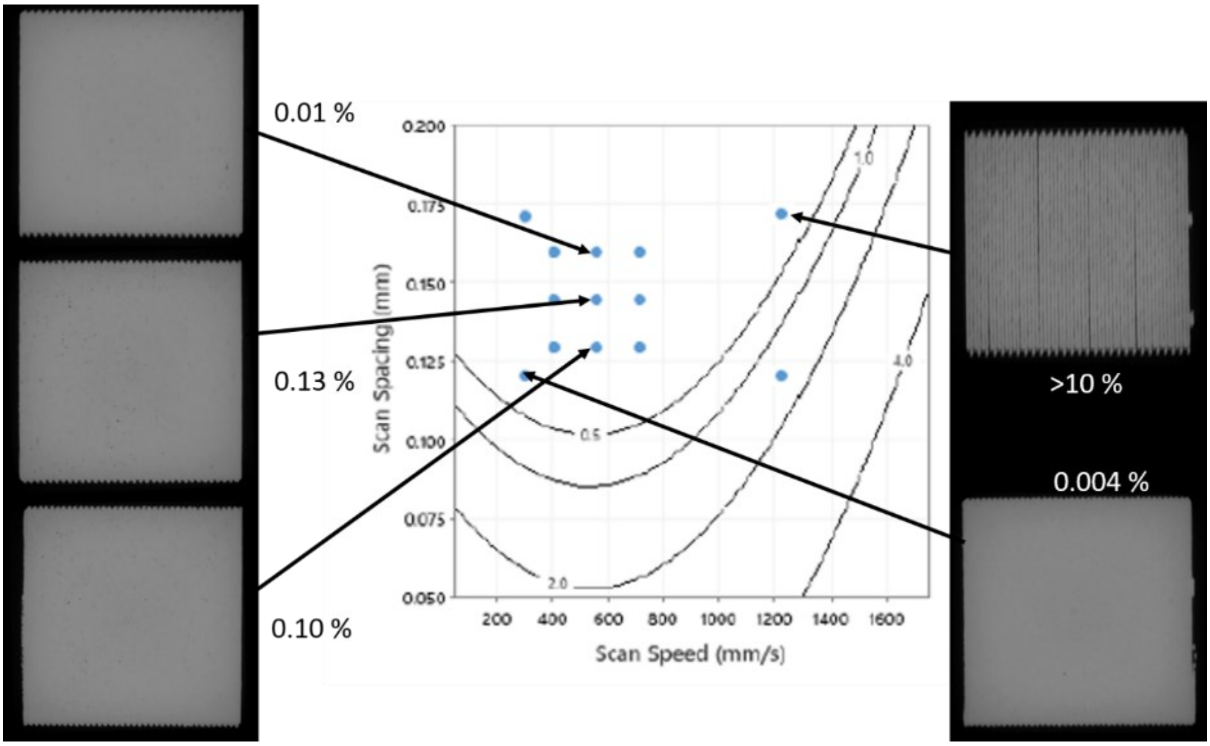

Figure 12: Slices of CT data illustrating the difference in porosity detected for cuboid samples built with different laser scan speeds and spacing overlaid on an empirical model. The overall volume fraction of porosity detected is given in percent next to each slice data

From Figure 12 we can see that our predictive model for porosity was reasonably accurate for all four of the specimens tested with scan speeds below 600 mm/s. However, the sample tested with the high scan spacing and speed produced a very poor sample, with gaps between individual melt tracks clear to the eye. Porosity for this sample was measured to be greater than 10 %, despite the model predicting < 0.5 %.

For the three samples tested with a 550 mm/s scan speed the relationship between porosity and scan spacing was not clear, with a small rise followed by a fall as the spacing was increased. Conversely, the lowest porosity was found with the lowest scan spacing (0.12 mm) combined with the lowest speed (317 mm/s) making it difficult to draw definitive conclusions from this data alone.

To examine whether the settings used were appropriate for a range of sample sizes, the build was repeated but using smaller samples, namely 6.5 mm diameter cylinders with 20 mm height. From the results shown in Figure 13 the measured porosity has changed significantly. The link between scan spacing and porosity is clearer for this set of samples, with higher scan spacing’s resulting in reduced porosity when the speed was constant. However, the overall porosity measured is very different to the cuboid samples. This is concerning and suggests that to fully link melt strategy to defect population, models must include a factor to account for geometry. This will increase the complexity, both in terms of model construction, but also in its experimental validation.

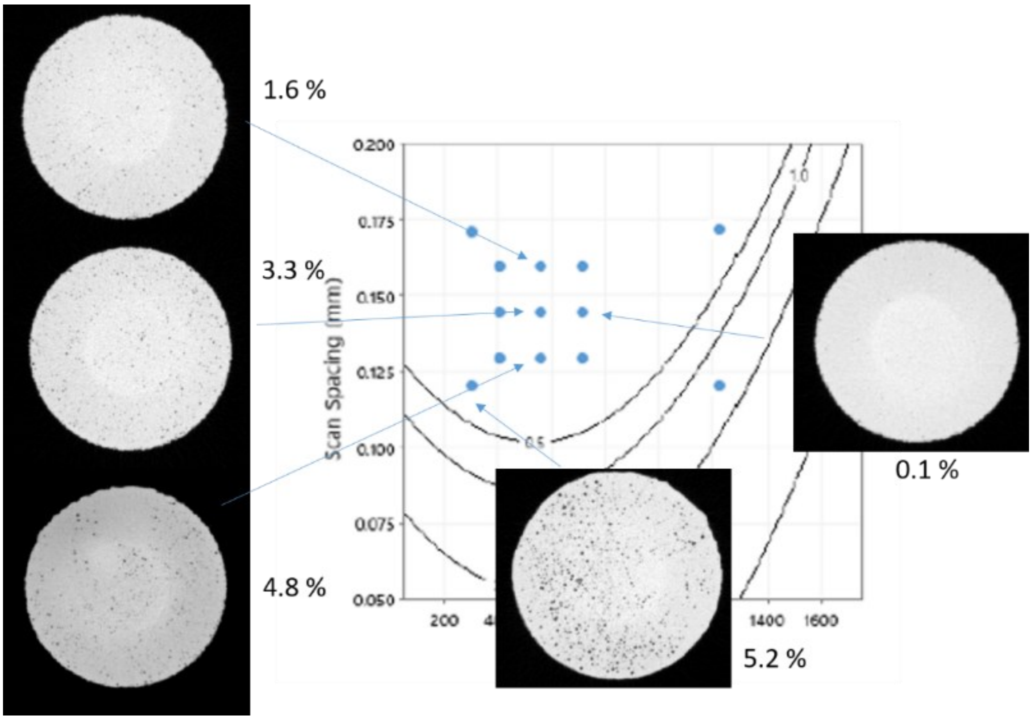

Figure 13: Slices of CT data illustrating the difference in porosity detected for cylindrical samples built with different laser scan speeds and spacing overlaid on an empirical model. The overall volume fraction of porosity detected is given in percent next to each slice data

Fortunately, potential reasons behind the model breakdown for the smaller samples can be inferred by examination of the defect types generated. Most defects were regular, i.e., a low aspect ratio, Figure 13, and in some cases appear in a linear fashion. Given that the defects increased in frequency as the energy increased, we attribute them to boiled metal vapours, i.e., keyholes pores [31]. The fact these voids only appeared on the smaller sample may be explained by considering the reduced time for cooling due to the shorter laser scan length. In other words, the material is hotter when the laser hits it due to residual heat from the previous pass having less time to dissipate. However, we can conclude that despite the model making use of multiple published data, it does not well predict the properties of our AM parts.

Towards explaining poor model fits

Given the results from section 3.1, (the uncertainty in CT measurements) we know that CT can produce very different results depending on how it is analysed. Therefore, there is significant uncertainty in the literature reported values for porosity measured by CT. This is before we consider any inherent variation in the pore volume fraction due to the manufacturing.

To begin to quantify the uncertainty in literature data, information was gathered from the literature and used to manufacture samples that were identical in all reported process parameters. Other than the LPBF machine, all other reported settings were identical. The literature reported volume fraction was also noted. A comparison between the literature stated pore volume fraction and the volume fraction we calculated when conducting the Archimedes method on nominally identical samples is show in Figure 14.

There is clearly some difference between the published volume fraction and the volume fraction measured here of samples that were intended to be similar. It is most apparent for the samples where the literature data was collected by CT (hatched bars). For literature data collected by Archimedes, there is better agreement between our results and previous studies when the line energy was less than 0.19 J/mm, but above this value there is significant differences.

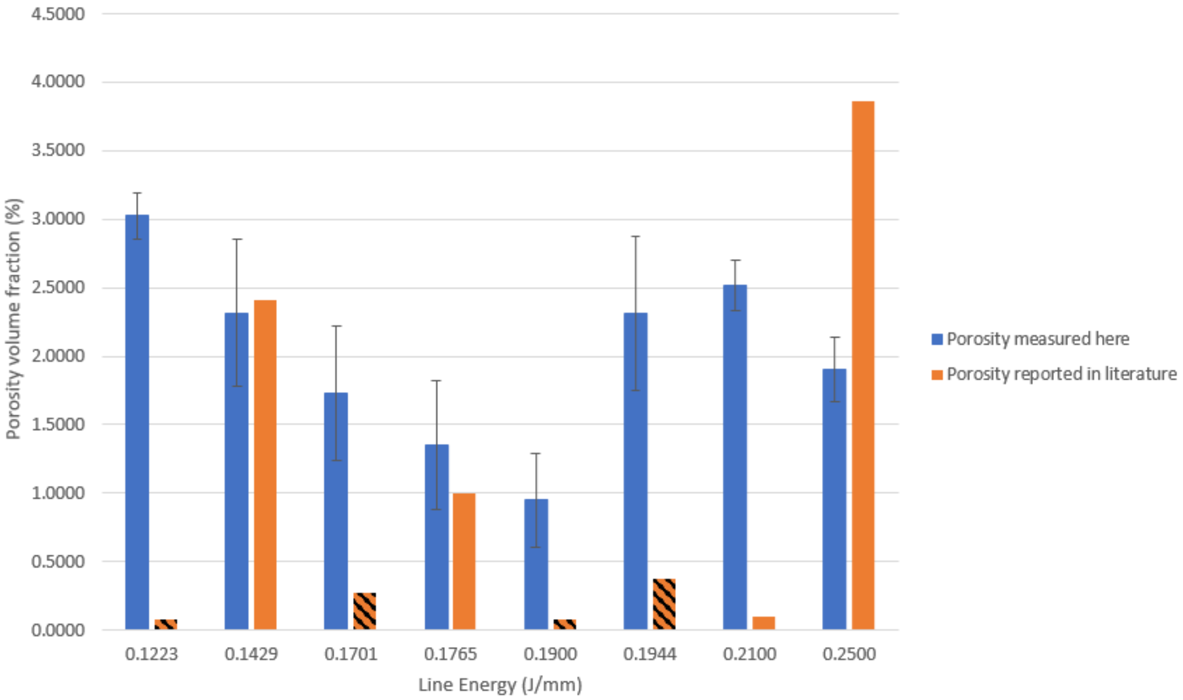

Figure 14: Comparison of literature data and our replications, solid bars indicates where the literature reported porosity measured by the Archimedes method, and hatched bars where it was reported by the CT measurement. The error bars indicate the standard deviation of 3 measurements.

This deviation between previous data and our data may be due to variations between machines, poor reporting of build settings, or errors in measurement. Regardless of the cause, it is concerning that we cannot use existing data to predict porosity in new samples. Overall, this may indicate that the statistical models we based on published external data may be of limited use to predict porosity.

Given that we found that we could more closely replicate literature porosity values measured by Archimedes, this suggest that this data is more likely to be comparable across studies. Clearly, with the limited data available here we cannot make definitive conclusions, but it suggests that when harvesting literature data preference should be given to Archimedes data, which avoids the subjectiveness of CT outlined in the previous section.

When we examine the literature data collected in this project, we note that it is approximately half was collected by CT and half with Archimedes. There is also limited data recorded using microscopy. The overall mean volume fraction porosity recorded with all measurement techniques was 2.6 %, but the mean for CT data was 0.8 % and for Archimedes was 4.8 %. The spread of data was also very different, as exemplified by Figure 15. We suggest that this is not due to the measurement technique. Rather given the greater cost associated with CT, it is expected that it is mainly used for high density samples, whereas Archimedes is used for the lower density samples.

However, we know that the same CT data can result in order of magnitude differences when processed by different users. When this is combined with the small changes in porosity that CT is typically used to measure, it suggests that we cannot rely on it to produce repeatable results.

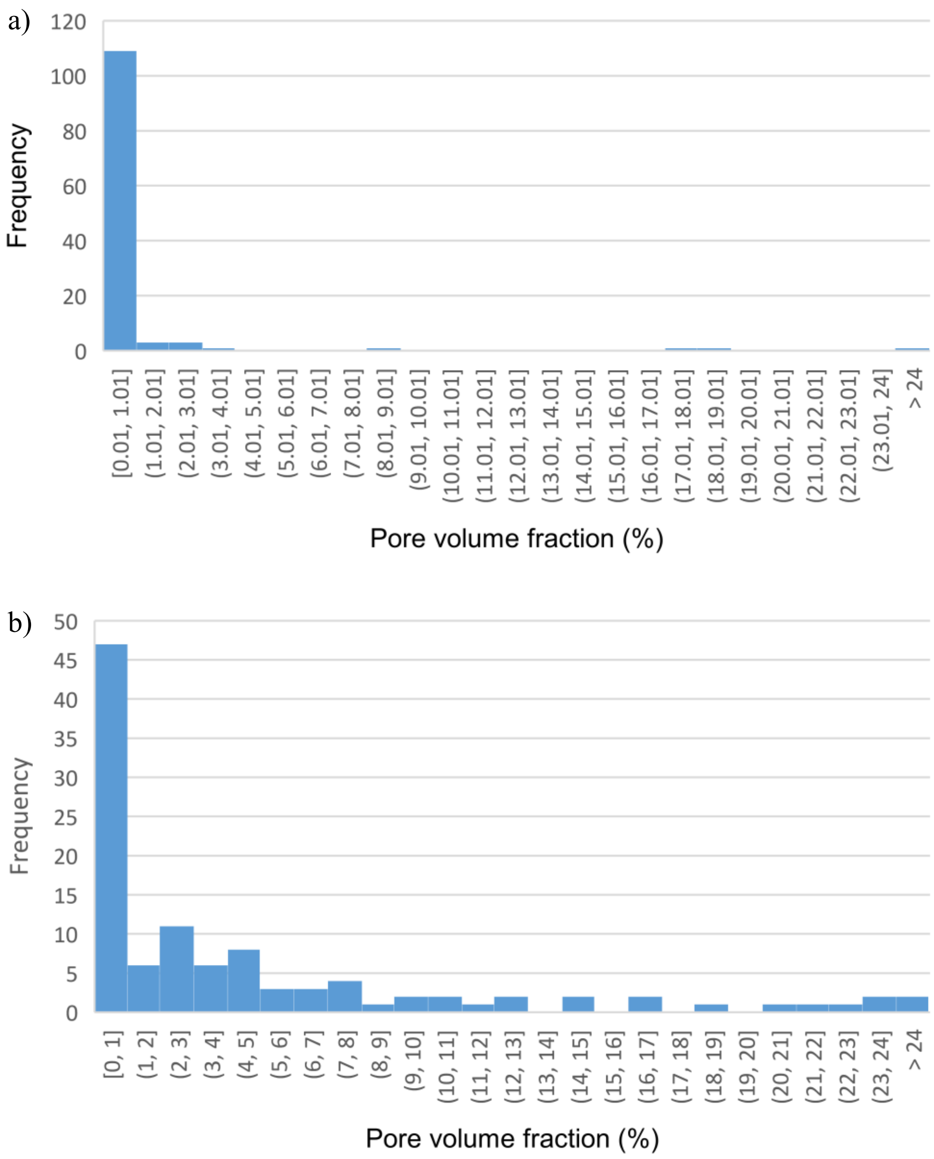

Figure 15: Histogram of porosity values recorded in the literature. (a) measured by CT, and (b) measured by Archimedes.

In addition to measurement uncertainty, there is also an inherent scatter in the porosity observed in the process. When samples were manufactured using standard settings (60 µm layer thickness) at different location in a Renishaw AM250 bed, there were significant differences in the volume of porosity measured by X-ray CT. Figure 16 shows how the measured volume fraction porosity changes with location in the bed. The schematic is not to scale and the total build plate is 250 mm by 250 mm.

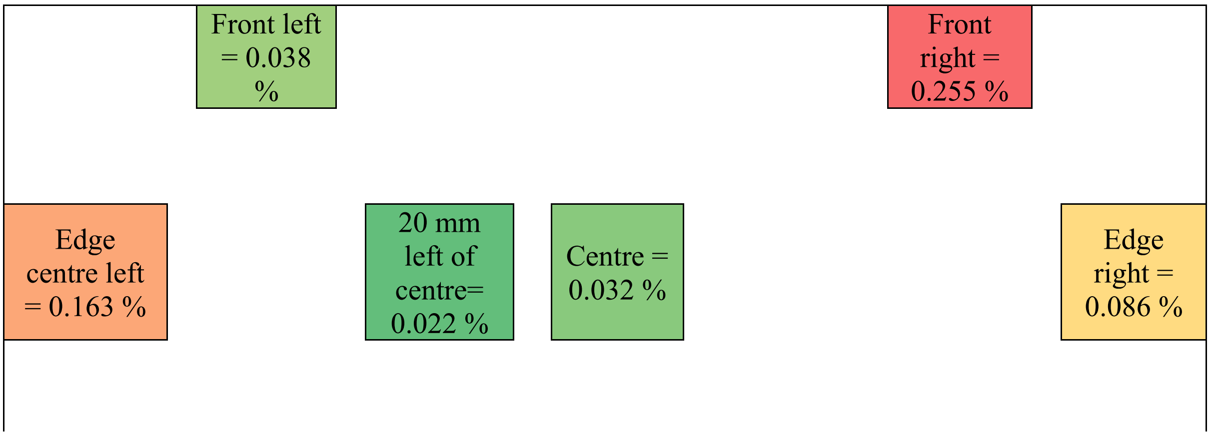

Figure 16: Schematic diagram showing the measured porosity variation with location in the build. Only half the built plate is shown for clarity

It is apparent that two samples were found to contain significantly more voids than the others, namely the edge centre left, and the front right samples. The standard deviation of the measurements (0.09 %), is larger than many of the measured values. Visual inspection of the data (Figure 17a) reveals that the edge centre left sample contained a large crack which severely impacted the void quantification. In contrast, the front right sample (Figure 17b) contained a much higher number of irregular voids than the centre sample (Figure 17c). This was despite all samples being manufactured with identical settings.

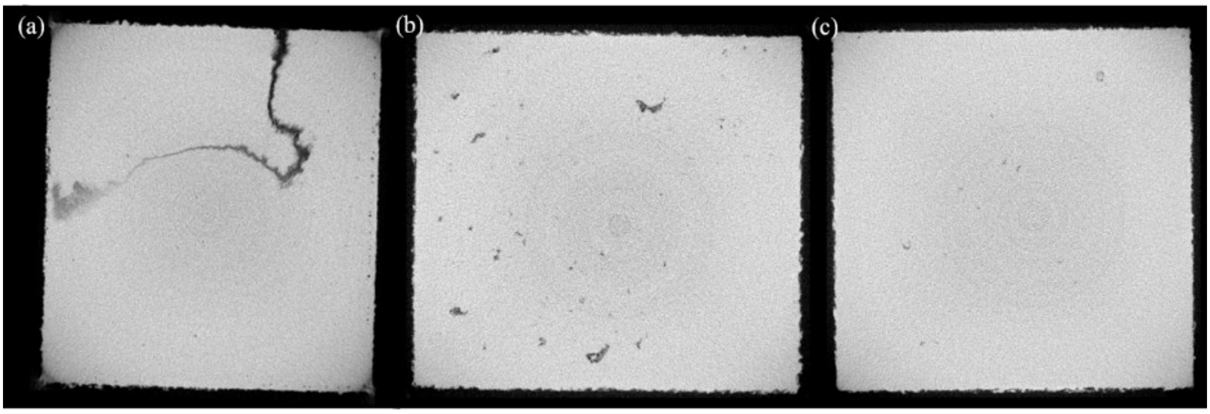

Figure 17: Example slices of X-ray CT volumes of samples produced with standard Renishaw themes from (a) the edge centre left; (b) front right; and (c) centre of the build plate.

This variation in porosity depending on position in the bed may go some way to explaining why some literature data could not be replicated. Furthermore, when a second manufacturing cycle was carried out, the standard sample was found to have a slightly lower volume fraction (0.02 %) than found in the previous build (0.03 %), despite using the same parameters in the same location.

Effect of post AM heat treatment on porosity

Careful alignment of the pre and post stress relief CT data has allowed the equivalent diameter measured as built to be plotted against the equivalent diameter measured after stress relief treatment (Figure 18). Of the 63 pores identified, 61 were found to have increased in size following heat treatment. The two that were not found to grow were both small and thus the relative error in the pore measurement was higher. A linear trend line explains much of the change observed ($R^2 > 0.99$) and is described by equation (10). It implies that smaller voids tended to grow more than large voids.

$$\phi_{SR} = 0.9754 \cdot \phi_{AB} + 1.5354 \tag{10}$$

Following heat treatment, the overall volume fraction porosity was found to have increased by 13 %. This is less than the change in volume fraction noted by repeating the same build. Therefore, we consider that heat treatment is unlikely to contribute significantly to the scatter.

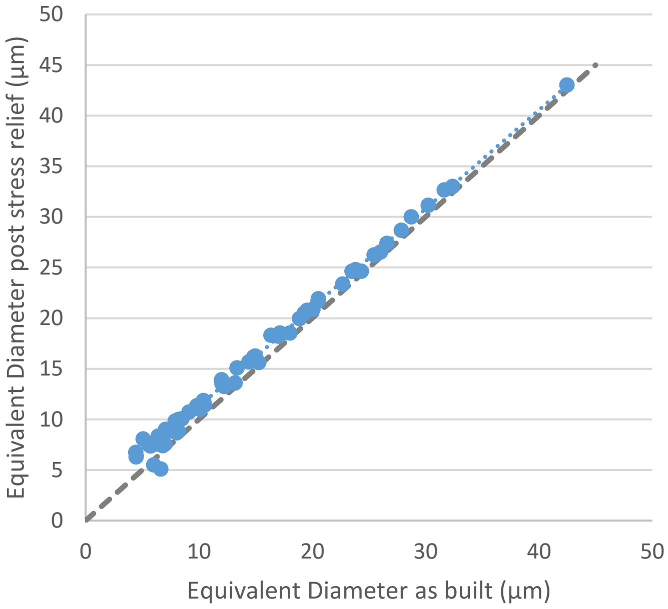

Figure 18: Comparison of measured pore sizes as-built and after stress relief heat treatment.

Development of dimensionless numbers and porosity model

During this project several studies have been published suggesting new dimensionless numbers that can be applied to PBF to help link process parameters to porosity and other properties, e.g. [32]–[34]. This can help reduce the complexity of equations used to describe the relationship between process parameters and offers the possibility of generating relationships that can be applied to multiple materials [29]. Gan et al. [33] have suggested that normalising the energy density by the energy required to melt (E_0^*, equation 8) can be enough to predict whether samples will fully melt. This equation is identical to that formulated by Thomas [29] via a different method. Combining this equation with the energy normalised by the energy required to vaporise/keyhole the material (KeL_d, equation 11), they produce a model they show can adequately predict the pore volume fraction in titanium, stainless steel and nickel alloys (Figure 19).

$$E_O^* = \frac{\eta \cdot q}{v \cdot h \cdot l} \cdot \frac{1}{\rho \cdot C_p \cdot (T_m - T_o)} \quad (11)$$

$$KeL_d = \frac{\eta \cdot q}{v \cdot r_b^2} \cdot \frac{1}{\pi \cdot \rho \cdot C_p \cdot (T_m - T_o)} \quad (12)$$

Where η, ρ, C_p, T_m, T_0, and T_v are the absorptivity, material density, specific heat capacity, melting temperature, powder bed temperature and melting temperature respectively.

However, inspection of equation (11) reveals that, for a single material, the right-hand side would be constant, and thus the normalised energy density proposed is directly proportional to the standard energy density. Several studies have confirmed that the relationship between porosity and energy input in LPBF is not straightforward, with many individual factors also influencing the volume porosity [38-41]. Gan et al. use limited data for each material, and unfortunately when we applied our data, we found more significant scatter. However, it should be noted that given the critical nature of r_b^2on the keyhole number (12), and the poor reporting of this value, we cannot properly test their hypothesis.

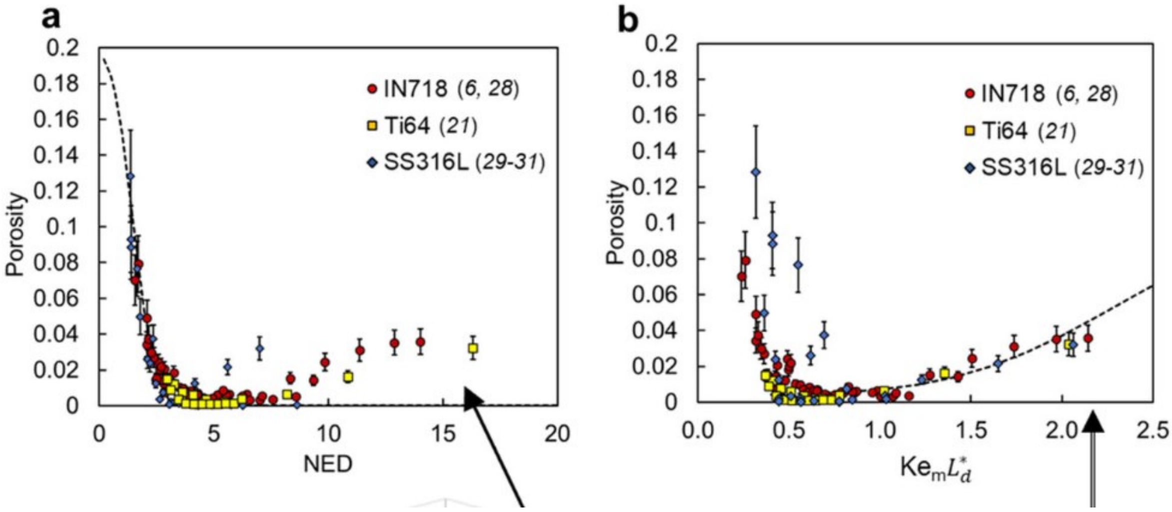

Figure 19: Normalised numbers for porosity prediction proposed by, and reprinted from, ref. [33], (a) normalised energy density, and (b) normalised keyhole number

We can however use the methodology proposed by Gan et al. to inform our model development. It is obvious that there is some minimum level of energy required to fully melt the material, which is what both Thomas et al., and Gan et al. have attempted to define. However, they neglect to include the effect of the latent heat of melting (L_m), so we modify their equation to include this (equation (13)) in our normalised energy to melt (E_m*).

$$E_m^* = \frac{\eta \cdot q}{v \cdot h \cdot l} \cdot \frac{1}{\rho \cdot (C_p \cdot (T_m - T_o) + L_m)} \tag{13}$$

E_m* can thus be considered a ratio of the delivered energy over the energy required to melt the material. We can also use the vaporziation number proposed by Gan et al., equation (12) to predict whether the material is likely to keyhole. Unfortunately, we have limited data regarding the effect of focus, given the lack of reporting of its value in the literature.

Thomas et al., normalised hatch spacing and layer thickness by the laser spot diameter. However, an alternative approach is available by using an equation proposed by Tang et al. [37]. This may be complementary rather than a replacement. They suggest that the maximum melt pool width (W) for alloys that do not have high conductivity (such as titanium) is described by equation (14).

$$W/2 \approx \sqrt{\frac{2 \cdot \eta \cdot q}{e \cdot \pi \cdot v \cdot \rho \cdot C_p \cdot (T_m - T_0)}} \tag{14}$$

We can use this equation to normalise the distances set in the control software, for example hatch spacing (h^*_{melt}) or layer thickness (l^*_{melt}), equations (15) and (16) respectively. To reduce the equation complexity, the unitless constants, e, π and 2, have been combined.

$$h_{melt}^* = \frac{h}{\sqrt{\frac{\eta \cdot q}{e \cdot \pi \cdot \rho \cdot v \cdot c_p \cdot (T_m - T_0)}}} \approx 2.066 \cdot h \cdot \sqrt{\frac{\cdot \rho \cdot v \cdot c_p \cdot (T_m - T_0)}{\eta \cdot q}} \tag{15}$$

$$l_{melt}^* = \frac{l}{\sqrt{\frac{\eta \cdot q}{e \cdot \pi \cdot \rho \cdot v \cdot c_p \cdot (T_m - T_0)}}} \approx 2.066 \cdot l \cdot \sqrt{\frac{\rho \cdot v \cdot c_p \cdot (T_m - T_0)}{\eta \cdot q}} \tag{16}$$

h^*_{melt} and l^*_{melt} can thus be considered a ratio of the distance between laser passes and the size of the melt pool. From Figure 20a&b it is clear that if $h>W$ (i.e. $h^*_{melt} >1$) or $h=W$ (i.e. $h^*_{melt} =1$), there will be significant lack of fusion voids generated. The minimum level size of melt pool required to fully melt the material is given in Figure 20c, based simply on Pythagoras theorem. Thus, we can define a dimensionless number (d^*_{melt}) to consider the ratio between this distance and the melt pool size, equation 17.

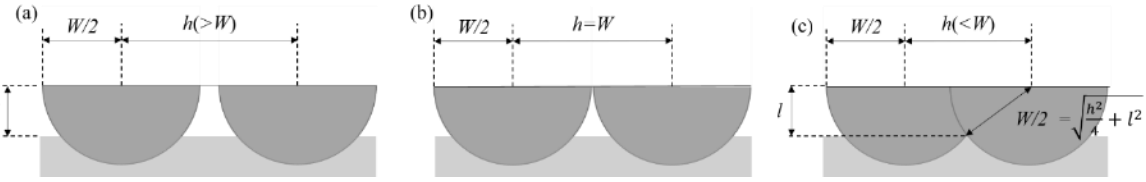

Figure 20: Relationship between melt size and lack of fusion defects. Here the laser traverse direction is normal to the plane of the page. The minimum size for a hemispherical melt pool is a function of the hatch spacing and layer thickness.

$$d^*_{melt} = 2.066 \cdot \sqrt{\frac{h^2}{4}+l^2} \cdot \sqrt{\frac{\rho\cdot v\cdot c_p\cdot(T_m-T_0)}{\eta\cdot q}} \qquad (17)$$

Finally, the laser power can be normalised by the amount of heat that is conducted away, as per equation (18), to give an indication of how much energy is lost relative the amount of energy input.

$$\therefore q^*_k = \frac{\eta\cdot q}{k\cdot(T_m-T_0)\cdot h} \qquad (18)$$

Here we have used the hatch spacing as a length term, but this could be replaced by any characteristic length, e.g., layer thickness or beam diameter.

Material property values were taken from Gan et al. [33] and an absorption of 0.5 was assumed to plot these numbers against porosity volume fractions (Figure 21). Many of the plots show similar trends and at this point we are still working to establish the most important numbers for predicting porosity. However, some trends in porosity can be explained by considering what the numbers represent.

Perhaps the simplest trend identifiable is the amount of energy input not being sufficient to fully melt the material ($E_m{}^*$). Note that this number must be greater than 1 to account for the remelting of previous layers and hatch tracks to ensure good bonding, here around 3 seems to be required. Similarly, the relative melt pool size must be large enough to properly bond between tracks. Encouragingly, when d^*_{melt} rises above 1 this is associated with a rapid decrease in density, as would be expected from the schematic in Figure 21. We should avoid over interpreting this as the number of assumptions in calculating the melt pool size is large. What is clear is that d^*_{melt} must be kept below some value to ensure proper melting. We can also see a similar trend to that observed by Gan et al. [33], with higher porosity values as *KeLd* rises above a certain value. The major caveat being that in many cases the beam diameter was not stated explicitly in the literature source and instead was inferred from other data.

The dimensionless numbers also give some clues as the best arrangement of parameters in an empirical equation, e.g., the powers by which to raise parameters. If the dimensionless numbers themselves are used, any mathematical operations can be performed on them and they will still produce a number with the correct units for porosity, i.e. unitless.

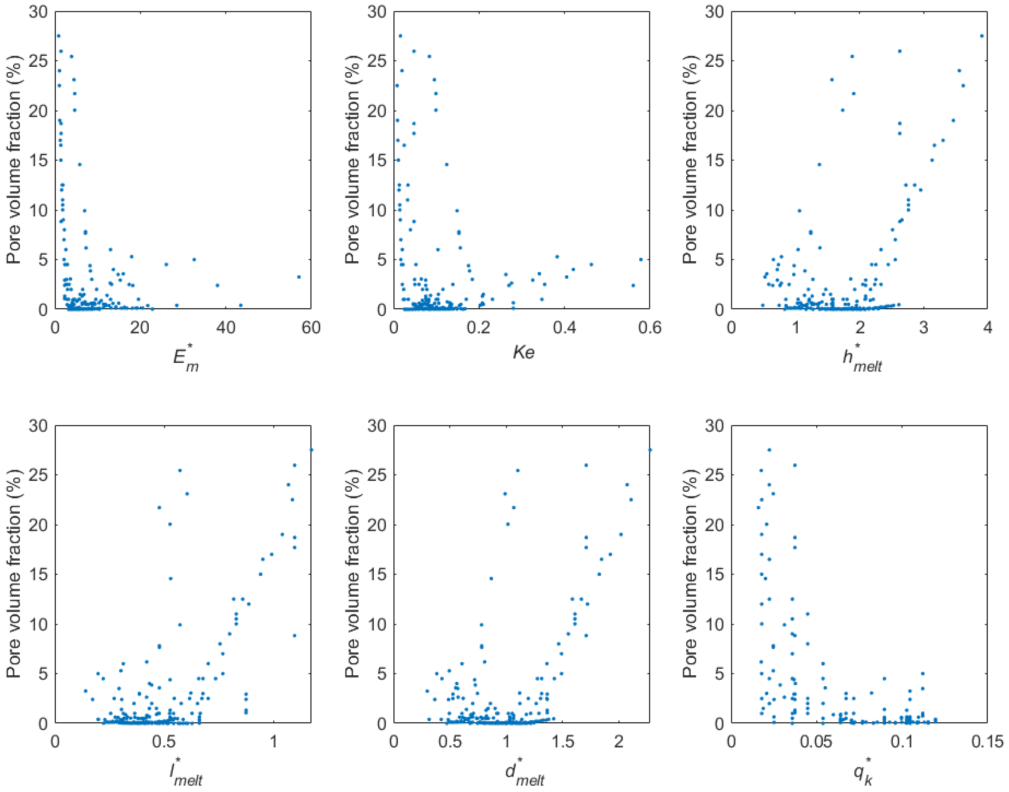

Figure 21: Pore volume fraction against dimensionless numbers derived.

Given the issues raised about comparing porosity measurements from different techniques the data was split based on the measurement method. Several regression models were created, for both CT and Archimedes data. Perhaps the most promising was a model using just two inputs ($d*$ and $l*$) with an R^2 of 91 % to predict porosity reported by Archimedes. Inspection of equations 15 and 17 implies that the hatch spacing and layer thickness (both to raised power 1) have a greater influence on porosity than either speed or power (raised to power 0.5 and -0.5 respectively).

To ensure that the model was producing physically explainable results the expected porosity has been calculated for a range of laser powers and speeds (via $d*$ and $l*$), resulting in the contour plot shown in Figure 22. While the expected positive relationship between power and speed resulting in a low porosity is visible it does not indicate that higher speeds associated with a lower line energy. The reason for the contradiction with our earlier result is currently unclear, and is one of the subjects of study for the PhD student working on this project in their remaining time.

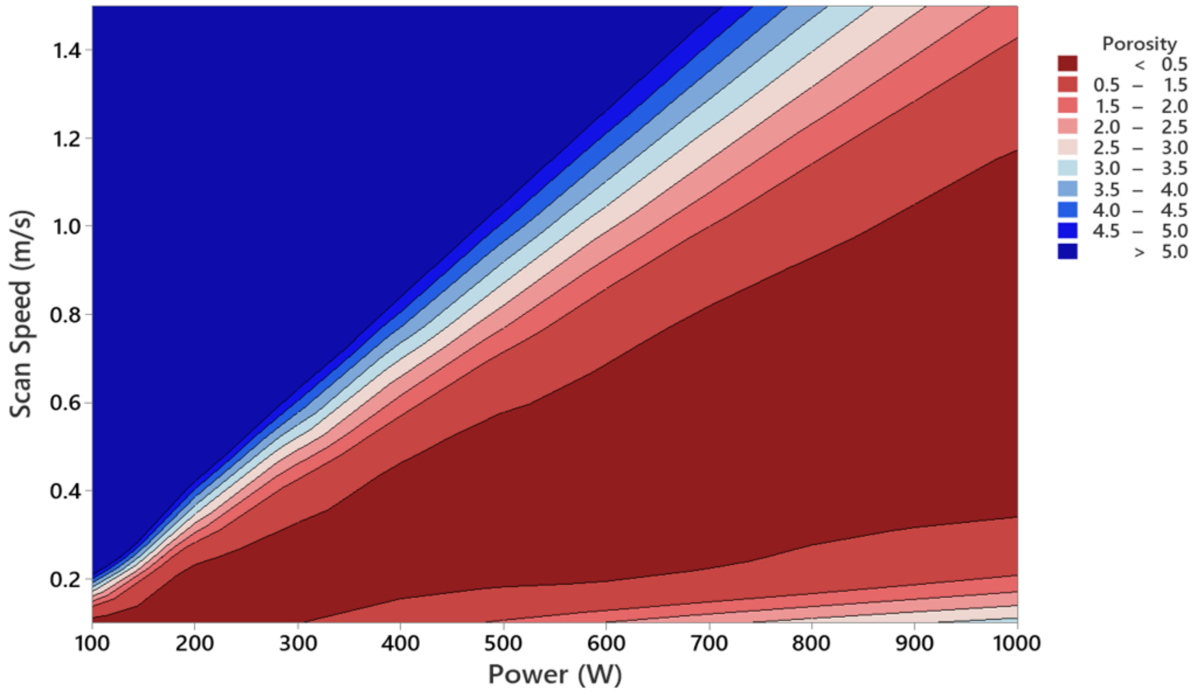

Figure 22: Example plot of porosity predicted by dimensionless number regression model

Experimental evaluation of melt strategy effect on defect population

A study of the effect of melt strategy on overall porosity volume fraction was conducted by increasing and decreasing energy inputs away from the manufacturer recommended for a Renishaw system operating with a 30 µm layer thickness. The variation of porosity volume fraction measured by CT is presented graphically in Figure 23, and numerically in Appendix A. 30 cylindrical samples of diameter 6.5 mm and height 20 mm were produced. For all hatch spacings, the most porous samples were those produced with a low exposure time and high point distance. Several tested parameter sets were measured as having a lower volume fraction than the Renishaw recommend settings, typically when a higher exposure time and/or lower point distance were used.

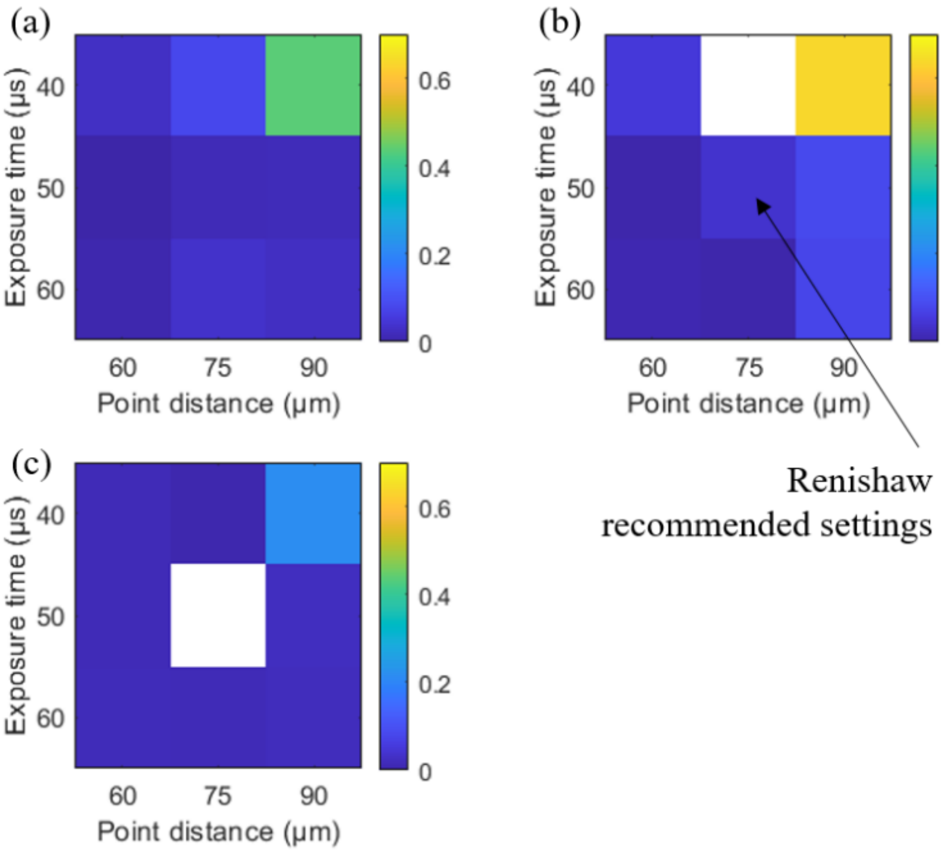

Figure 23: The effect of exposure time and point distance on measured pore volume fraction indicated by color for samples produced with a hatch spacing of (a) 52 µm, (b) 65 µm, and (c) 78 µm. White area indicates samples that have not been analysed.

From Figure 24 it is apparent that line energies less than 0.1 J/mm were unable to produce dense samples, regardless of the hatch spacing. This aligns well with our meta-analysis of previously published literature. However, for all the conditions tested, the overall fraction remained below 1 %, and when using an energy density of greater than 68 J/mm^3 the porosity remained below 0.1 % (Figure 24). A range of energy densities can be used to produce high density samples.

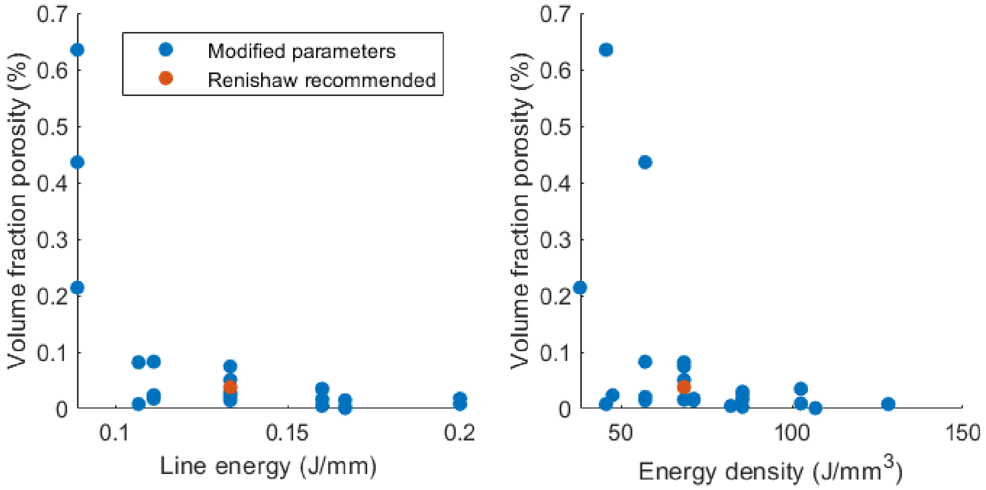

Figure 24: Measured pore volume fraction for samples produced using a Renishaw AM125 plotted against (a) line energy, and (b) energy density.

Analysis was also conducted on samples manufactured with a 60 µm layer thickness. Before considering the defect population, it is worth acknowledging the large difference in energy density when working with the Renishaw recommended settings, with the 30 µm layer recommended to receive 68 J/mm^3 vs only 41 for the 60 µm layer. This casts further doubt on the use of the standard energy density equation to predict porosity, even when normalised.

When the hatch spacing was reduced from the standard value (0.095 mm) the overall volume fraction was found to increase in an approximately linear fashion (Figure 25a). However, it is notable that the increased number of pores associated with a 75 µm hatch spacing was still less than the number of pores found in the standard sample made on the previous build. In other words, the inherent scatted in the measured data was greater than the difference due to the hatch spacing. When the exposure time was increased from the Renishaw recommended standard (70 µs) the volume fraction porosity first very slightly decreased, before a showing a very significant rise (Figure 25b).

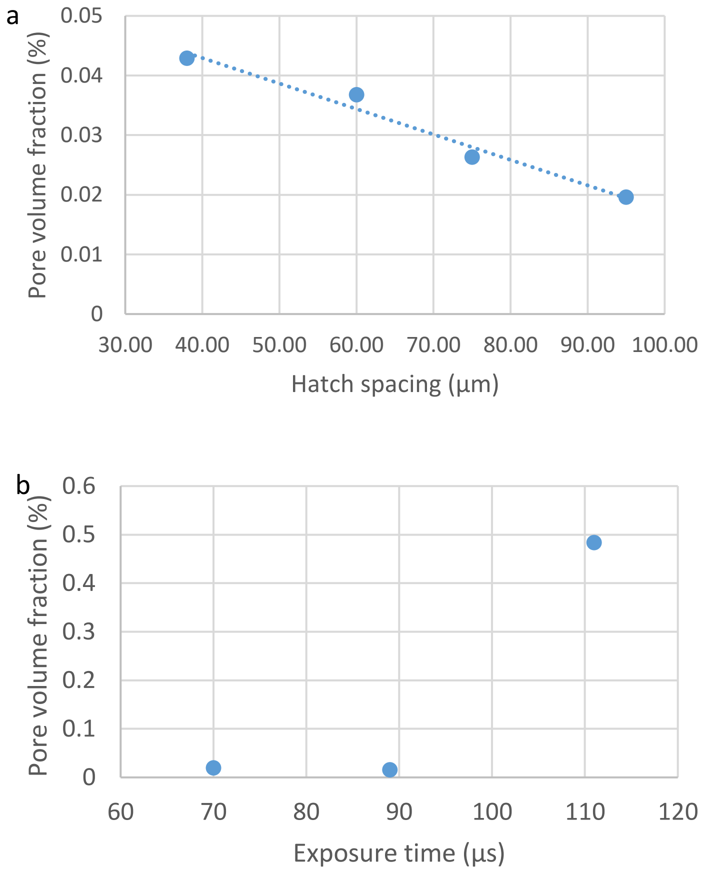

Figure 25: Effect of (a) hatch spacing and (b) exposure time on measured volume fraction porosity for a Renishaw system using 60 µm layer thicknesses.

When laser settings identical to those recommended by the EOS manufacturer were used with an Aconity system to produce small samples, CT analysis suggested a high-density sample (>99.99 %) was achieved. The full settings used are provided alongside the volume fraction in Table 5. To ease interpretation the volume fraction of porosity measured by CT is plotted against energy density in Figure 26. By increasing the energy density from the EOS recommended level, we were able to achieve an approximate halving of recorded volume fraction porosity.

Table 5: Manufacturing settings, calculated energy inputs and pore volume fraction for sample based on strategies similar to that recommended by EOS. Layer thickness and beam diameter were held constant at 0.03 mm, and 0.1 mm, respectively.

Power (W)	130	170	130	170	130	170	130	170
Scan Speed (mm/s)	1000	1000	1250	1250	1500	1500	1250	1250
Scan Spacing (mm)	0.1	0.1	0.1	0.1	0.1	0.1	0.08	0.12
Line energy (J/mm)	0.130	0.170	0.104	0.136	0.087	0.113	0.104	0.136
Energy density (J/mm3)	43.333	56.667	34.667	45.333	28.889	37.778	43.333	37.778
Volume fraction (%)	0.008	0.001	0.627	0.002	2.493	0.073	0.278	0.049
Notes				EOS suggested				

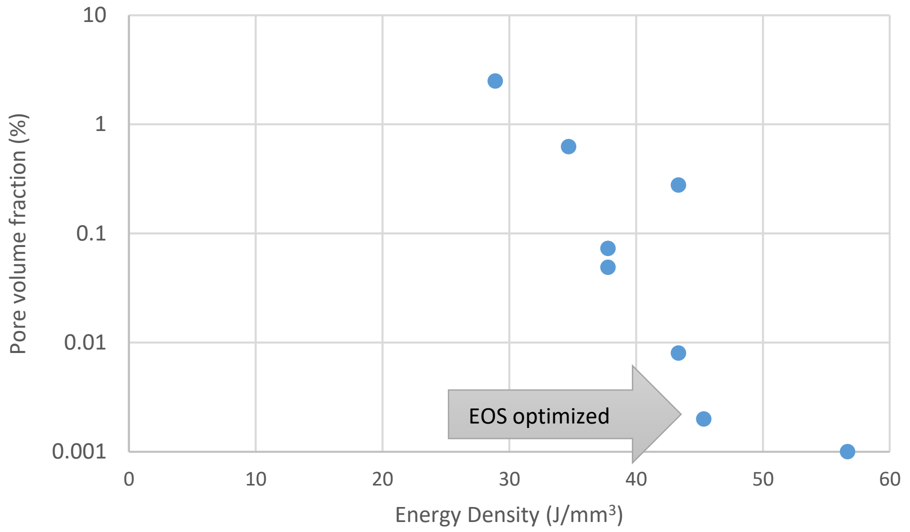

Figure 26: Porosity against energy density for samples based around EOS settings

This result aligns with our previous observations of the Renishaw system, which also showed a potential reduction in pore volume fraction when the energy was increased. This was the case when analysed by the student working full time on this project. In both the Renishaw and EOS case, the slight absolute change to the porosity, and the significant uncertainty outlined in section 3.1, we cannot be sure that this is a true reduction. Conversely, in both cases, reducing the energy density did result in an increase in pore volume fraction. This suggests that these two manufactures have chosen default settings at the lower end of what is acceptable for porosity. This may be to increase the build speed of the machine as well as reduce the energy requirements. Furthermore, we cannot comment on how these settings would perform when used to produce larger components.

Effect of process parameters on defect characteristics

The histograms of pore sizes shown in Figure 27 are arranged by exposure time (columns) and hatch spacing (rows) for the samples manufactured with a 60 µm layer thickness with a Renishaw system. The three different energy densities used are also indicated. No significant difference can be observed between the standard sample (energy density = 41 J/mm^3) and those produced with an energy density of 52 J/mm^3. For the 65 J/mm^3 samples differences start to appear. The high exposure time leads to a greater number of small defects, while the low hatch spacing leads to a greater number of larger defects.

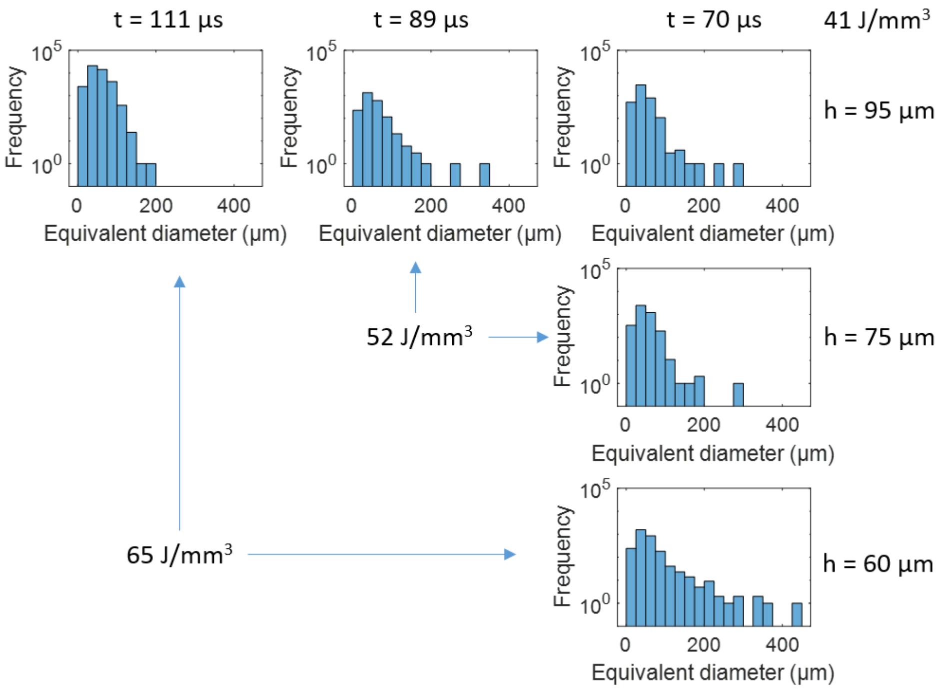

Figure 27: Histograms of pore sizes recorded for various manufacturing strategies

To visualise the different defect types a 3D reconstruction of the standard sample and high exposure time and low hatch spacing are shown in Figure 19a. Two defect types can be observed in the standard sample (t = 70 µs, h = 95 µm), and examples of each are shown enlarged in Figure 28b, where they appear as irregular voids (i) and reasonably spherical voids (ii). For the high exposure time sample, the number of near spherical voids increased, with an example shown in Figure 28b (iii). In contrast, for the low hatch spacing sample the number of irregular voids increased, Figure 28b (iv).

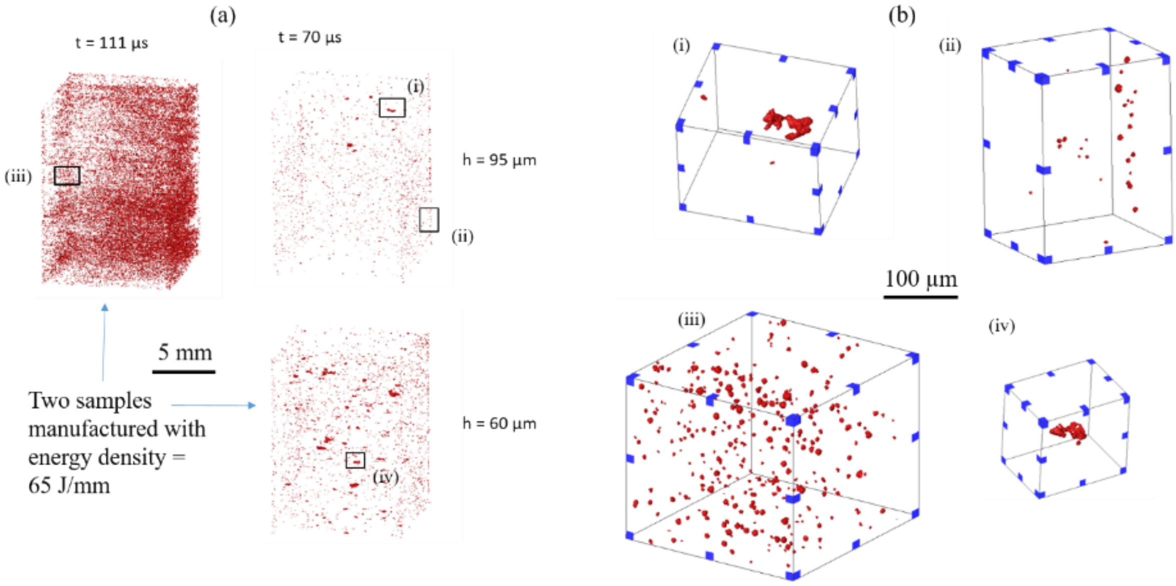

Figure 28: 3D visualisation of segmented X-ray CT data of (a) whole specimens; and (b) zoomed in on specific defects indicated in (a).

The change in defect appearance is reflected in the calculated sphericities. From the 3D histograms in Figure 29, it can be observed that once again there is not a significant difference in the distributions of defect sizes against morphologies between samples made with energy densities of 48 J/mm^3 and 52 J/mm^3. However, for the highest exposure time the number of voids with low sphericities but relatively small size increases, indicated by the circle marked (i). For the low hatch spacing, the number of larger irregular voids increases, shown as (ii) in Figure 29.

Given their morphology, and the fact they appear when the laser is moving slowly, appearance we attribute the regular defects to keyholing [35]. The irregular defects are more challenging to define, and at first appearance could be classified as lack of fusion. Given they appear at high energies this is unlikely to be the case, instead they may be due to powder denudation caused by increased vapour plume as observed by Bidare et al. [36].

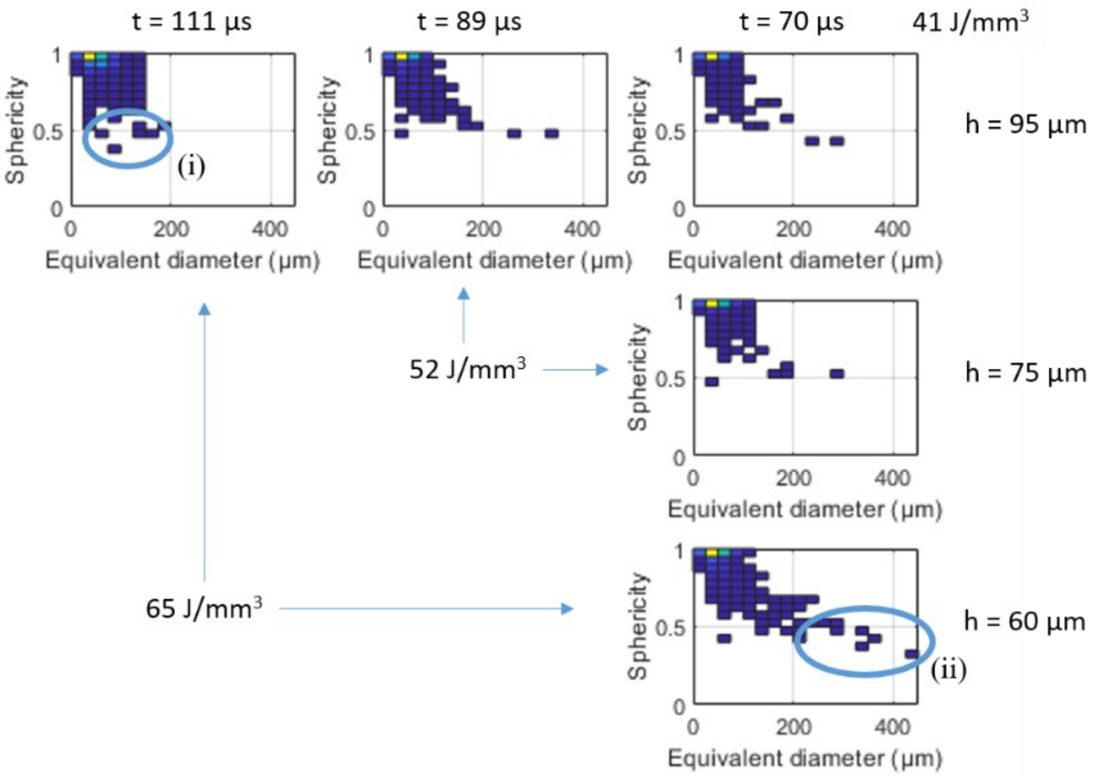

Figure 29: 3D histograms showing the relationship between build parameters and defects' size and morphology. Note that data has been normalised for ease of reading, i.e. the colour represents the relative not absolute number of defects in each segment.

A similar difference in the defect morphology could be observed in the 30 µm layer Renishaw samples (Figure 30). Interestingly, when a lower energy was applied, very irregular defects, similar in appearance to those noted with a high energy and low hatch spacing above. However, given the reduction in energy density compared the standard sample, we suggest these are caused by lack of fusion rather than powder denudation.

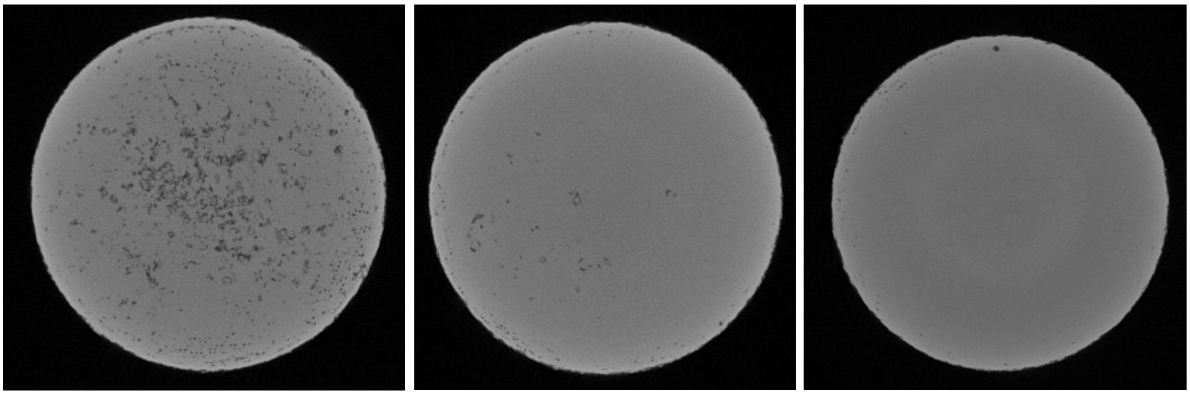

45.6 J/mm^3 **68.4 J/mm^3** **102.6 J/mm^3**

Figure 30: Example CT slices showing (L-R) low, standard, and high energy conditions

When the energy input was increased round defects were observed (Figure 30), which we again attribute to keyholing. The keyholes were particularly prevalent at the edge of the sample where the laser turns back on itself. This would effectively decrease the laser speed and bring it within the region known to produce keyholes [35].

It is notable that the standard sample (E = 68.4 J/mm^3) with a 30 µm layer, was significantly less porous than a sample produced with a similar energy density and 60 µm layer thickness. Again, the weakness of using energy density alone is highlighted, as the energy density of the standard 30 µm layer sample is very much greater than the 60 µm layer samples discussed above. A similar energy density (41-46 J/mm^3) produces good quality material with a 60 µm layer, but very porous with a 30 µm layer.

From the slices in Figure 30, a distribution in porosity can be observed. To quantify this, the variation in pore volume fraction is plotted with distance from the surface in Figure 31. The method is described elsewhere [37]. In this case all three energy conditions show a peak around 0.3 mm from the surface before decaying to an approximately steady level of porosity further than 0.5 mm from the surface, albeit at a much higher level for the low energy sample.

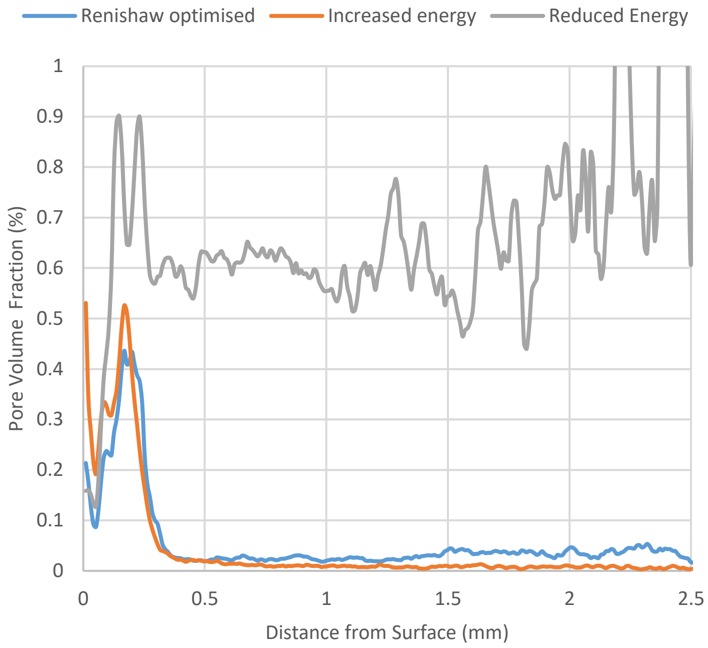

Figure 31: Distribution of porosity within samples manufactured with a Renishaw melt strategy and increased and decreased energy.

A similar analysis was conducted on the samples with a higher and lower energy than the EOS recommended settings, and is shown in Figure 32. When the speed is reduced (energy increased) not only does the overall volume fraction decease, but there also appears to be a significant reduction in the pore volume fraction in the first 0.5 mm from the surface. In contrast, when the speed is increased, there is a significant peak close to the surface, before dropping and then reaching a steady level of porosity. When considering the effect of pores on fatigue, this change in the distribution may be more important that the overall reduction in volume fraction as it may change the number of pores near the sample surface that can act as ready sites for crack initiation [26].

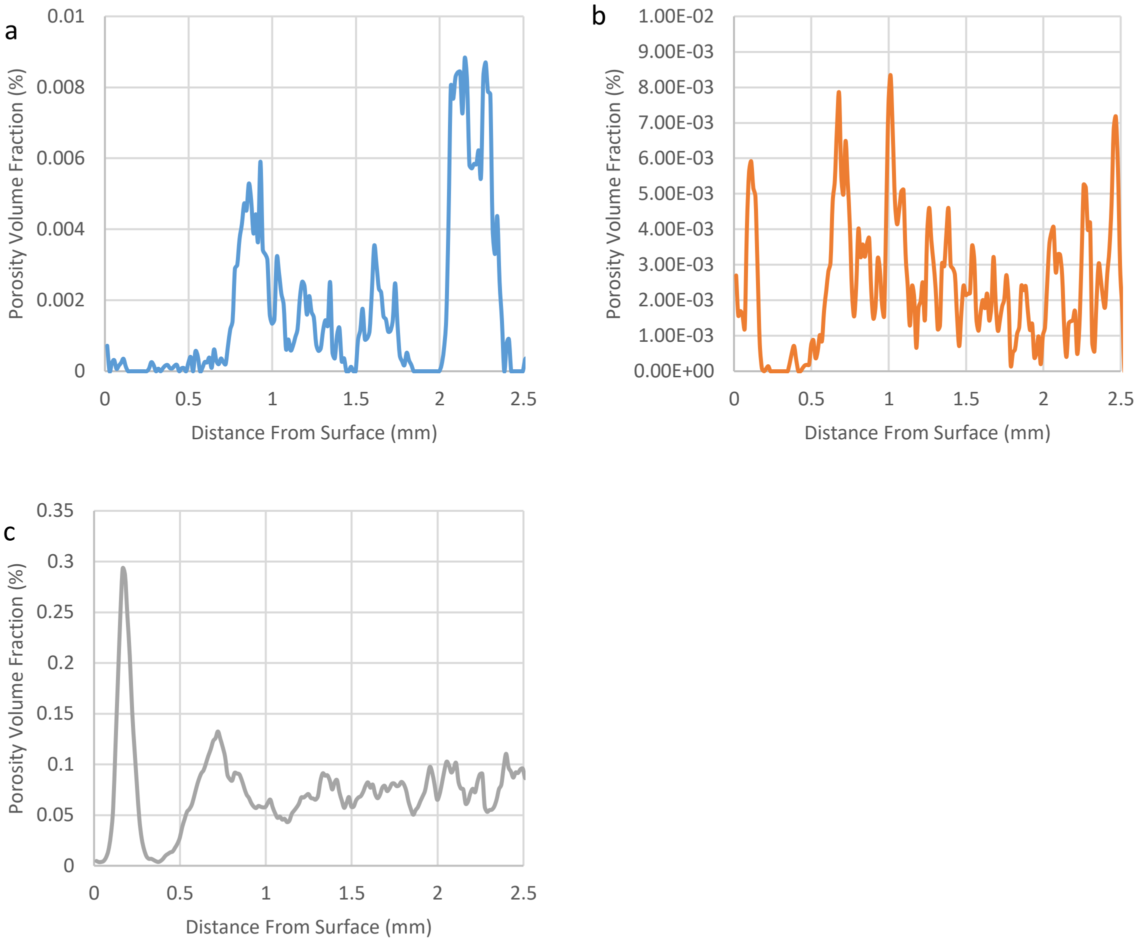

Figure 32: Distribution of porosity within samples manufactured with power of 170 W, and speeds of (a) 1000 mm/s, (b) 1250 mm/s (EOS standard) and (c) 1500 mm/s. Note different vertical axis scale in c.

From Figure 31 and 32, we can infer that the melt conditions are different in the outer 0.5 mm of material. This is unsurprising given the need for the laser, and associated mirrors with inertia, to slow from its maximum transverse speed to a stop and then reverse direction. If the power is not adequately compensated for, this can lead to changes to the line energy, which may result in this peak in porosity.

We can also conclude that removing 0.5 mm of material from our mechanical test specimens prior to testing (as has been done in this project) may well be removing the most porous part of the material. This may give a higher fatigue life than if less material were removed. In addition, it suggests that overbuilding titanium parts and then machining to remove material (i.e. more than a surface finish operation) may be a prudent move for any fatigue loaded LPBF components. Unfortunately, this means that the increased design freedom associated with AM is reduced as surfaces must be accessible by tooling.

3.3 Effect of defects on mechanical properties (TASKS7-10,12)

Overview of Stress life data collected.

From the S-N data plotted on Figure 33, the manufacturing strategy has a significant impact on fatigue life. Sample sets A, B, Aconity & EOS were manufactured with the same powder batch, on the same LPBF machine, and subjected to the same heat treatment following manufacture. Renishaw samples were manufactured using a different LPBF platform but subjected to the same heat treatment. Renishaw-HT were subjected to a higher heat treatment, which is likely to have resulted in a different microstructure.

The worst performing samples are those manufactured based on EOS settings. However, when examination of the fracture surface of the EOS samples, revealed an unusual morphology, atypical of a fatigue crack initiation and growth cycle. We believe that these samples had cracked during manufacture, likely due to the residual stress induced by the rapid cooling and delays between the sample manufacture and the heat treatment. Interestingly, despite experiencing the same manufacturing cycle, including heat treatment, the Aconity samples did not crack, which may indicate that they less prone to cracking. The Aconity settings were developed for this machine, which indicates the difficulties of developing machine agnostic laser manufacturing strategies.

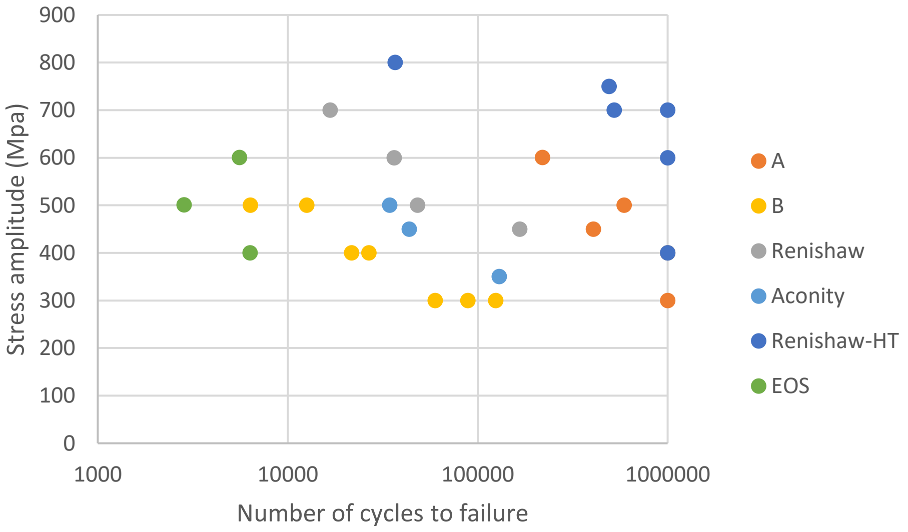

Figure 33: S-N data for AM samples tested build with a variety of stratergies. Testing was stopped when samples reached 1 million cycles.

The samples known to be very porous (B), were the second worst performing. The best performing where the Renishaw samples subjected to a higher heat treatment. In contrast the Renishaw samples subjected to the same heat treatment as the rest of the samples were marginally better lived than the Aconity recommended settings. Of the samples subjected to the lower heat treatment, set A (defined in this project) appeared to give the best performance.

The best performing material was the Renishaw material subjected to a higher heat treatment.

Fracture surface analysis

Of the 25 fracture surfaces examined, a pore could be identified as the initiating feature at 22 of them typical of PBF fatigue [21]. 20 of the pores were classified surface pores, i.e., within one of their diameter width of the surface. This was based on the work of classification used by Murakami [24]. Figure 34a, shows an example of a near surface pore that was still classified as a sub-surface pore. Various pore morphologies were observed, with some more regular than others. Surprisingly, early analysis suggests that the morphology of the pore did not affect the fatigue life. Instead, the size alone was important. However, investigation is ongoing to verify this.

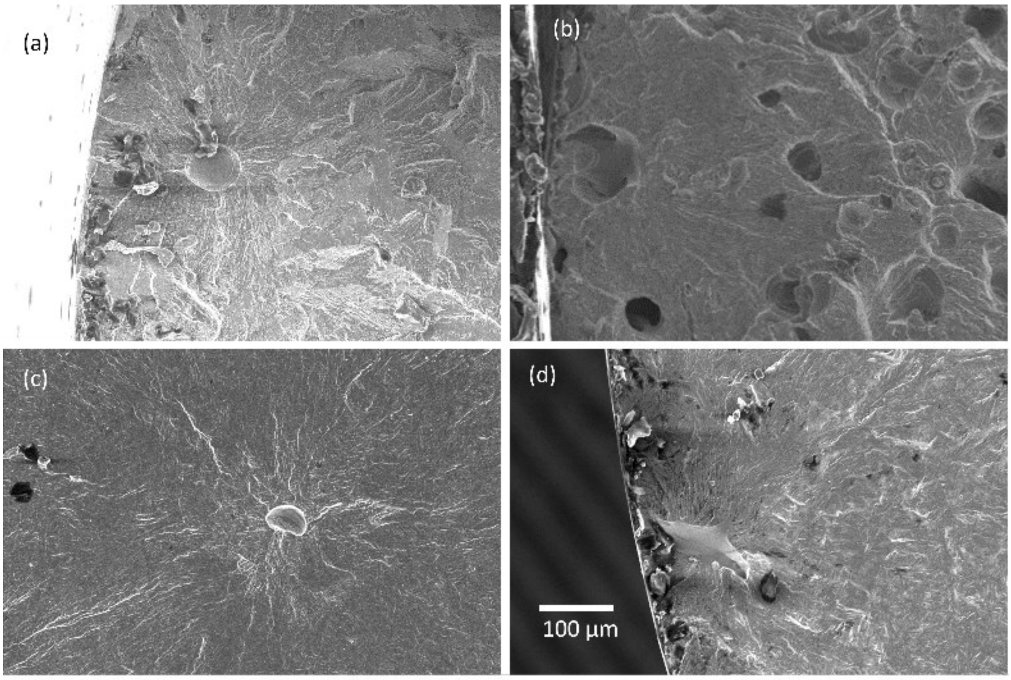

Figure 34: Examples of pores that lead to crack initiation. (a) a sub-surface pore from sample set A, (b) a surface pore from set B, (c) a sub-surface pore from a Renishaw sample, and (d) an irregular surface pore in a Renishaw sample

None initiating porosity

In addition to examining the pore that caused the fatigue crack via SEM, the CT data allows us to characterize the other pores that did not lead to cracking. If we can establish why a certain pore led to a crack, whereas all the others did not, it might help us design manufacturing and/or inspection strategies to remove or detect the worst pores. Unfortunately, current efforts to understand the unique features of the initiating pore have proved unsuccessful. Figure 35 is an example of typical data. It demonstrates the initiating defect was not the largest pore, nor was it the largest close to the surface. There were also pores that were both larger and more regular (higher aspect ratio) that did not lead to failure. Further work will be undertaken to see if we can extract useful information from this data (see future work).

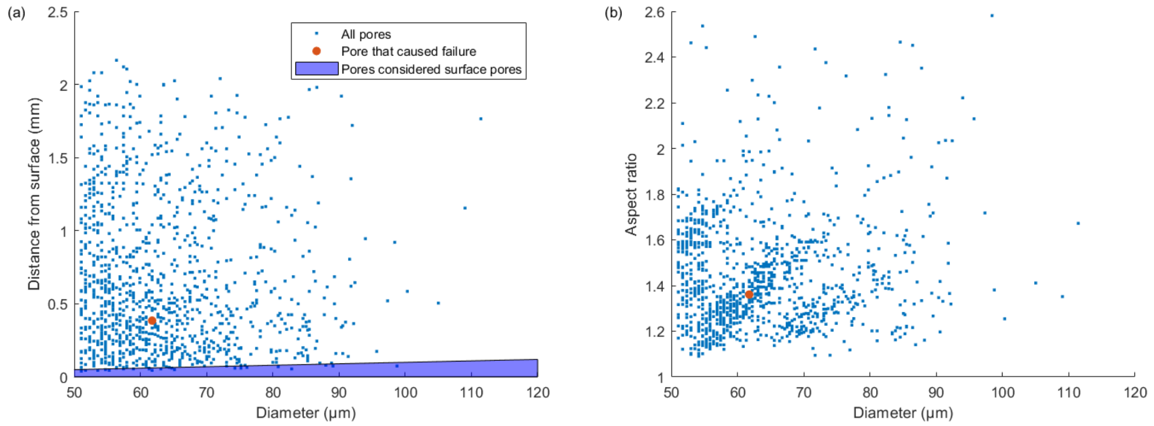

Figure 35: Porosity characteristics in fatigue sample from set A

Linking artificial defect characteristics to fatigue life

In order to understand more about the effect of defects on fatigue life, artificial defects in both wrought and AM titanium were used. From Figure 36a, where a traditional S-N curve has been plotted for the wrought titanium with laser drilled holes, the effect of hole size on fatigue life can be observed. An unsurprising link between intended hole size and fatigue life can be seen, with larger holes typically leading to shorter lives.

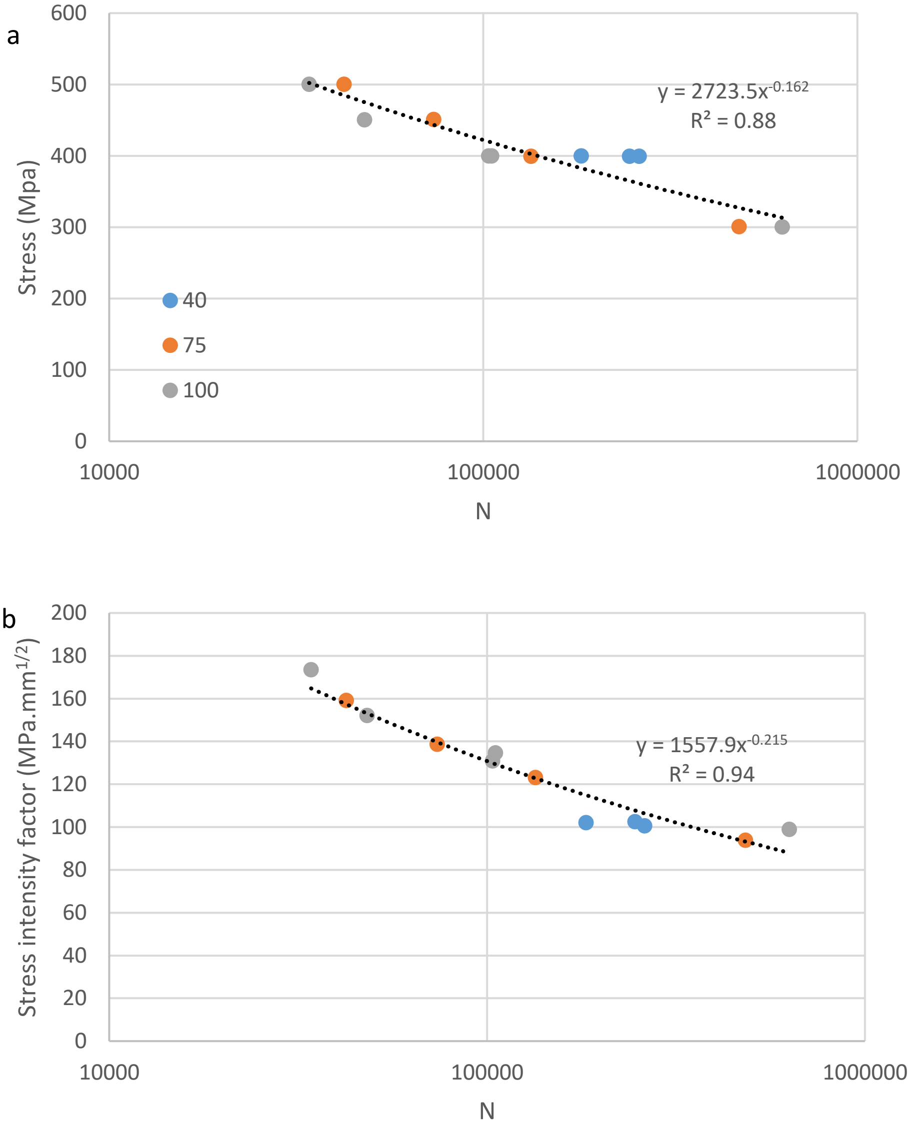

Figure 36: (a) Traditional, S-N curve for wrought titanium with laser drilled holes and standard Basquin's equation fitted. Color indicates the intended size of each hole. (b) SIF-N plot, with modified Basquin's equation fitted

Fracture surface analysis confirmed that the samples all broke from cracks initiated at the drilled hole. The SEM images were also used to measure the defect size and calculate a stress intensity factor for each using Murakami equation. The SIF provides a good correlation with the number of cycles to failure (Figure 36b). When equation 9 was fitted to the data, 94 % of the variation in SIF was explained.

To explore the effect of defect proximity the samples with two defects intended to be identical size were tested. The calculated SIF-N data Figure 37 was used to fit the modified Basquin's equation and we use this to compare different arrangements. This shows that when the defects are aligned with the stress, and spaced approximately one diameter apart, they behave almost identically to an individual defect in terms of their effect on fatigue life.

Conversely, when the defects are arranged normal to the stress, the fatigue life is lower than would be expected based on the SIF of a single defect. However, when the area of both defects is considered as is typically suggested [9], the SIF is greater than anticipated for this life. This suggests that two defects close to each other cannot be considered as producing the same stress intensity as a single large defect, but neither is information about the single defect enough to predict the fatigue life. This needs further experimentation before we can conclude the validity of this hypothesis. There may be a critical distance between defects we can identify.

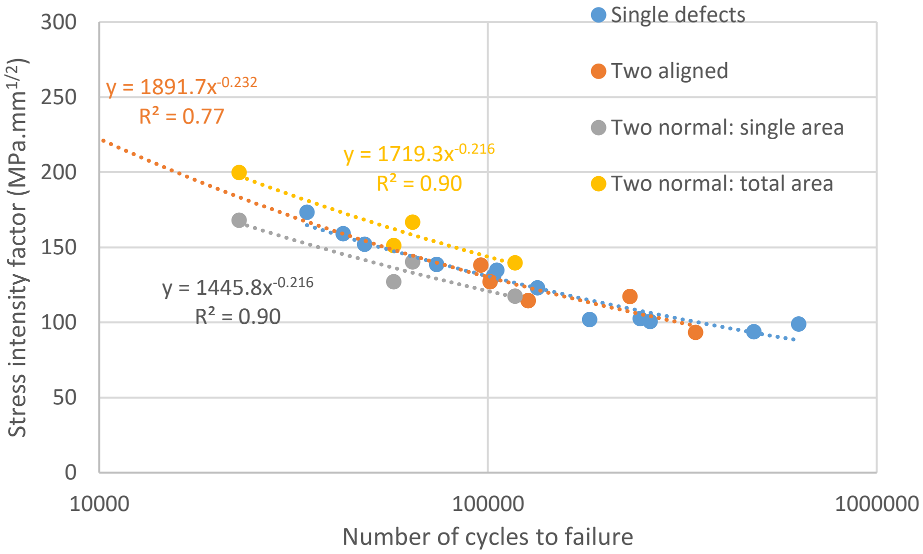

Figure 37: SIF-N curves comparing single and double artificial defects.

When artificial defects were introduced into LPBF AM material, (Figure 38), their estimated stress intensity factor had a less consistent impact on the fatigue life than wrought material. However, in general, for a given stress intensity, the AM material had a longer fatigue life than the wrought material. Looking at samples tested at the same stress, the Renishaw samples tended to have a longer life with the same defect area (exemplified in Figure 39). Given the sample geometry is identical, the increased life but with greater scatter is likely to be a function of the microstructure.

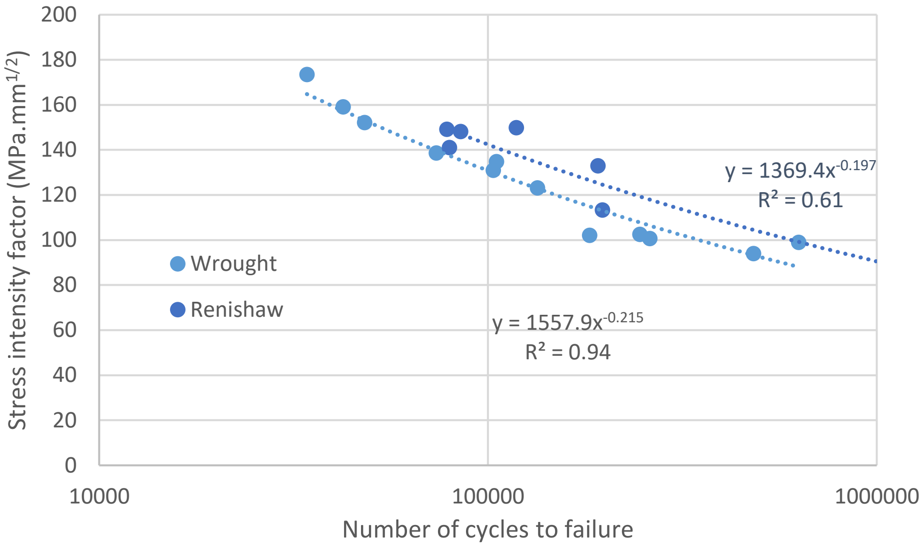

Figure 38: SIF-N showing response of defects on fatigue life for wrought Ti64 and AM Ti64

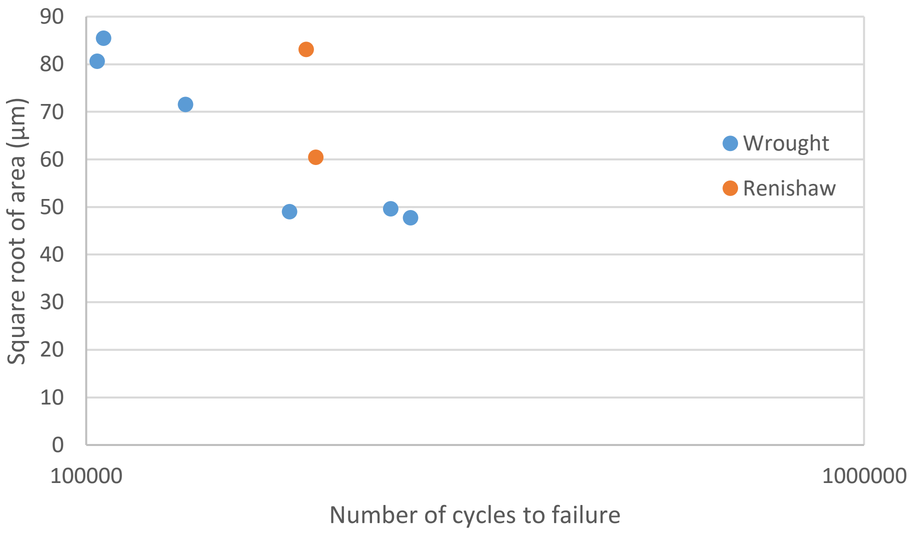

Figure 39:Cycles to failure against artificial defect size for samples tested at 400 MPa

In Figure 40, the microstructure of the wrought and LPBF material are shown. All sections examined exhibited a structure of primary alpha in a transformed beta matrix. However, the size and morphology of the grains is slightly different, which may have led to the increased fatigue life for the LPBF samples.

The increased scatter in the LPBF samples could be due to the microstructure or other "natural" pores interacting with the artificial defect. However, inspection of the fracture surfaces revealed that none showed other pores close to the crack initiation point. The fact that defects in line with the stress had no influence on the fatigue life, combined with the relatively low number frequency of pores in these samples, means that the presence of other defects can be assumed to be of relatively low importance in influencing the scatter. Therefore, we attribute this scatter to the local microstructure. For example, less consistent grain sizes and morphologies in LPBF material meaning some defects were aligned with grains with better aligned for slip and crack initiation than others.

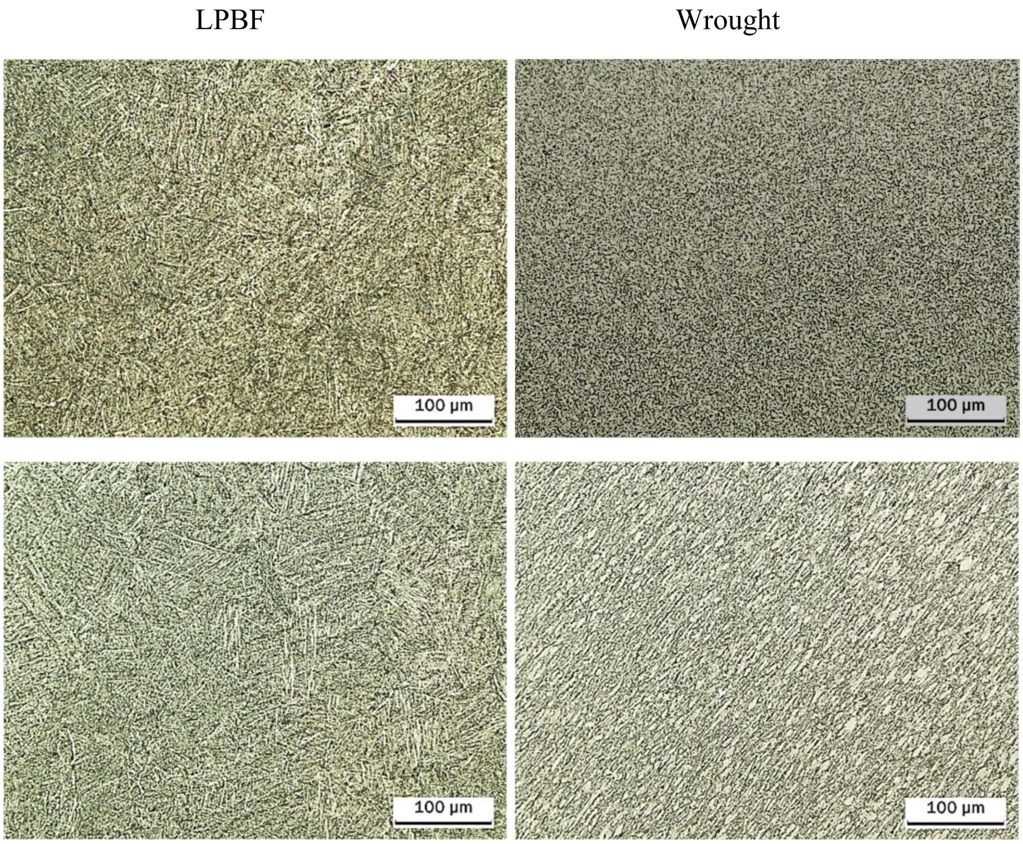

Figure 40:Left LPBF Ti-64, right Wrought Ti64. Images taken transverse to the sample test direction, above, and longitudinal, lower.

We can therefore conclude that even if the effect of the stress intensity of defects is accounted for, LPBF titanium may have a greater degree of uncertainty than conventionally produced material. This implies that that even if we could fully characterise the pores in an AM sample, there would still be scatter we could not account for. However, the performance is better than some conventional material.

Basquin's equation and correlating manufacturing to performance

Basquin's equation has been fitted to each sample set (Figure 41). However, the cracked EOS samples were excluded due to their differing failure mechanism and the Renishaw samples subjected to a higher heat treatment were removed. Samples that reached runout also were removed, and work is ongoing to use stepped testing to get failure data from these.

Each manufacturing strategy can be correlated to a particular form of Basquin's equation. However, generating a new S-N data for any change in laser settings would be a laborious undertaking. Some data is better predicted by this equation than others. The most scattered data is also the best performing material. We will attempt to explain the scatter by including a factor to account for pore size. This also has the benefit of avoiding the need to generate a new equation for any given laser settings and sample geometry.

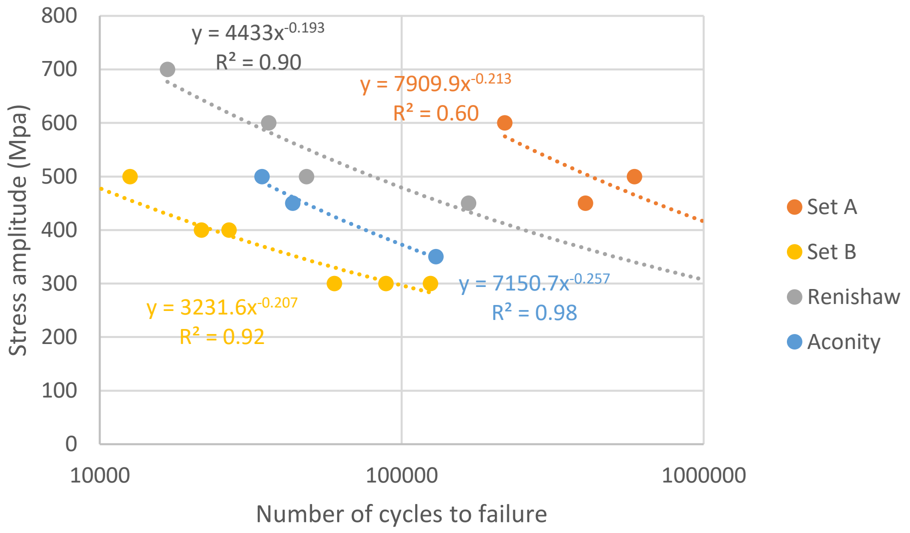

Figure 41: Basquin's equation fitted to fatigue data for various manufacturing strategies

Linking porosity to fatigue life

If we are to predict the life of any given component, understanding how an arbitrary sized defect would influence the fatigue life be useful. It is known that different areas of components can contain different volumes and frequency of defect [38], and as such may be reflective of the different samples tested here. Furthermore, we have demonstrated that the same settings can produce different results when applied in different parts of the bed, or in different builds. Therefore, to disentangle the effect of individual pores on fatigue, data has been combined to create an overall S-N curve for samples that failed from a pore (Figure 42a). Due to the high defect density sample set B are not included in the following analysis. The wrought samples with artificial defects are also shown for comparison and to illustrate the effect of the various ways of including the effect of defects.

Interestingly, of the B samples tested at 300 MPa, there was no correlation with the size of the pore at the crack initiation and the cycles to failure. We suggest this could be due to the high number density of pores, where some are close enough to behave as a single pore. Fracture surface analysis is ongoing to see if this can be quantified.

When a traditional S-N curve is plotted, the different machines used, alongside differing laser settings, mean that the link between stress and life is weak (low R^2). This is despite the fact that the same alloy and heat treatment was applied to each and all had a relatively high density. If this is due to different defect populations, taking account of the size of the defect that led to the crack may reduce the scatter.

When the stress intensity is calculated for each pore at the crack initiation, this makes some improvement to the fitted data (Figure 42b). However, when the normalised stress proposed by Masuo [9] is applied, there is a more limited improvement to the fit compared to just using stress (Figure 42c). This implies that while pore size is important, including a factor to account for the reduced life associated with surface pores is critical. The best fit achieved here was when combining the position constant proposed by Murakami with the normalised stress approach proposed by Masuo (Figure 42d).

Regardless of the method applied it has not been possible to significantly reduce the scatter. Although the normalised stress provides some explanation of the fatigue life, there is still significant scatter and many points lie far from the curve. Therefore, the benefit in terms of fatigue prediction is limited. In addition, the fitted curve gradient is quite low, which is concerning as it means that a small changes to the normalised stress would have a big impact on the predicted fatigue life.

With the limited data available here it is impossible to quantify the exact relationship, nor be sure about the relative contributions of each factor. This our data implies that the pore size is less important than indicated by the stress intensity factor, but the location of the pore is of importance, with pores near the surface associated with lower fatigue lives. Here we have estimated their increased contribution to the normalised stress using the values proposed by Murakami. These values were developed for a different situation, and so there is no reason to assume their validity, but without significantly more data we cannot make any reasonable estimations about better numerical values.

Our data from "natural defect" suggests that when using pore size ($\sqrt{A_n}$) to predict fatigue life it should be raised to the power $^1/_6$, not ½. We can see that the artificial defect data, also shows an improved fit when using the $^1/_6$ exponent, which corroborates our much more scattered "natural" LPBF defect data. This gives us reassurance that the lower exponent is worth considering.

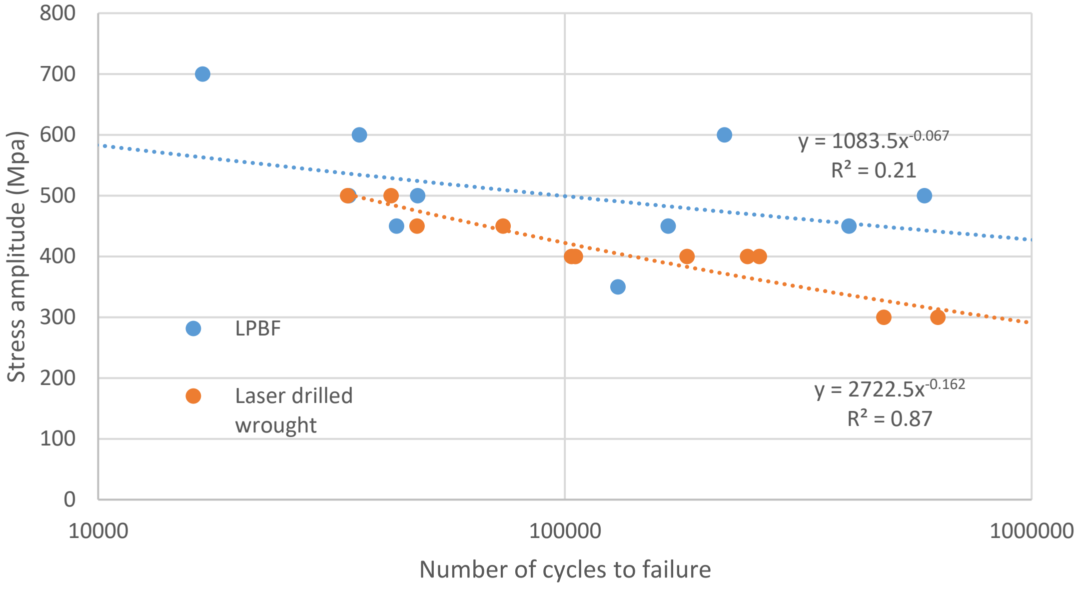
800
700
600
500
400
300
200
100
0
Stress amplitude (Mpa)
10000
100000
1000000
Number of cycles to failure
LPBF
Laser drilled wrought
y = 1083.5x^-0.067
R² = 0.21
y = 2722.5x^-0.162
R² = 0.87

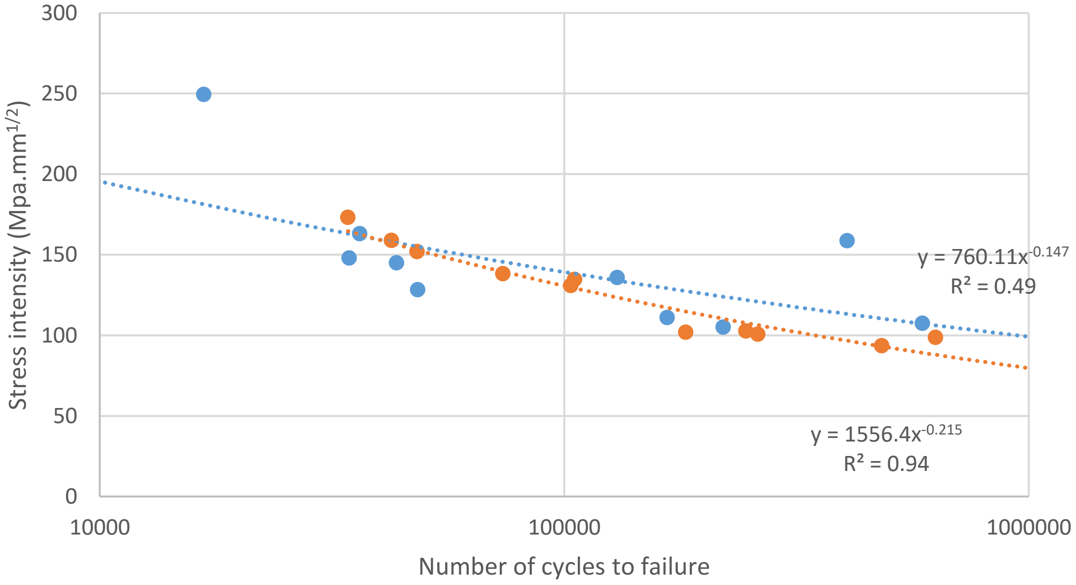
300
250
200
150
100
50
0
Stress intensity (Mpa.mm^1/2)
10000
100000
1000000
Number of cycles to failure
y = 760.11x^-0.147
R² = 0.49
y = 1556.4x^-0.215
R² = 0.94

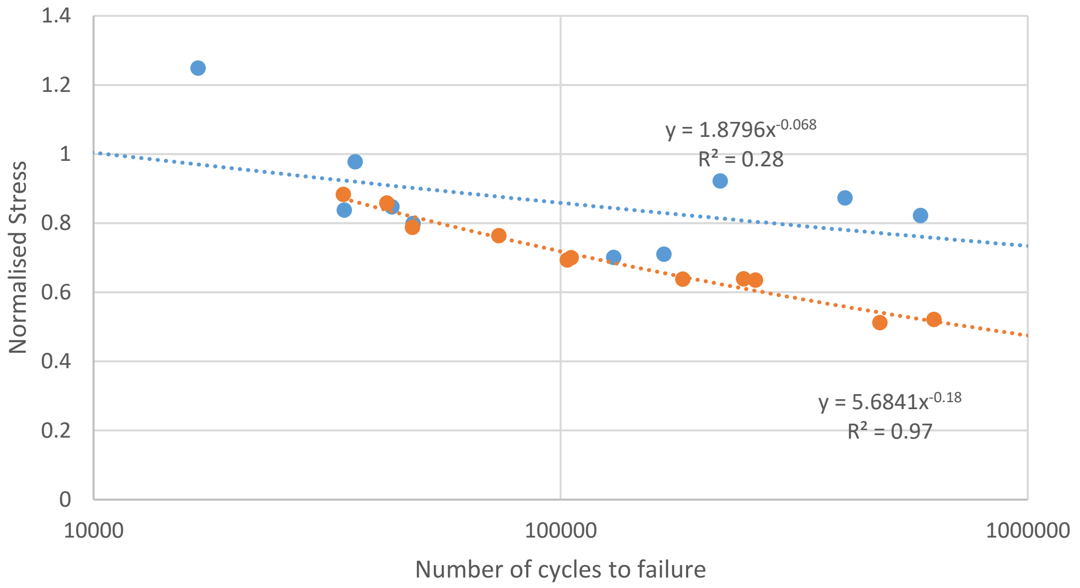

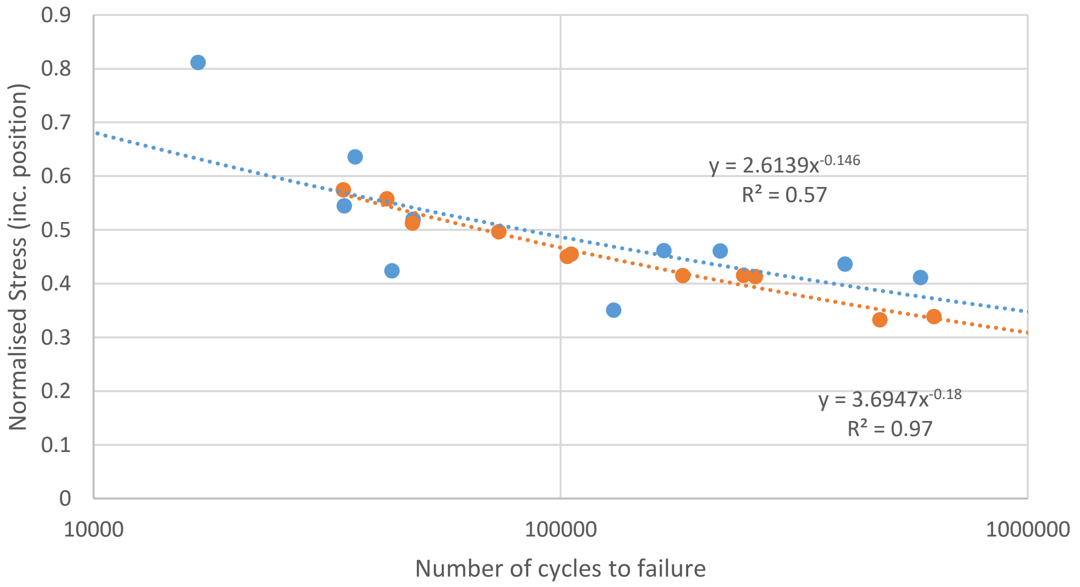

Figure 42: Fatigue life of laser powder bed fusion samples manufactured with different laser settings and plotted against various predictors.

4. Conclusions

A research effort has been conducted to link manufacturing to performance for LPBF titanium samples. Studies have been conducted into the detection limit of X-ray CT including the uncertainty in numerical results, how manufacturing influences the porosity generated, and how different manufacturing strategies influence the fatigue behaviour. Attempts have been made to rationalise the different mechanical responses by consideration of the porosity in samples.

TASK1

Significant work has been done to understand the uncertainty in X-ray CT measurements. Unfortunately, the results reveal significant, apparently random, error/differences between users looking at the same data. This has obvious implications when relying upon literature reported CT data to predict porosity levels in LPBF. In addition, when 3 data sets about 3 samples were provided to users, there was disagreement about which sample had the least porosity, which means that we cannot even assume that if published work was repeated, we would arrive at the same optimised conditions.

TASKS2-5

A statistical fit to published data has provided insights into the links between manufacturing and porosity. However, when we attempted to recreate samples that were nominally identical to those reported in the literature, we found a different porosity to that previously reported, especially when the literature data was reported by X-ray CT. This casts further doubt on the usefulness of compiling multiple sources of data from various sources. We also found that the difference between nominally identical samples made on a single machine could be greater than the differences observed when changing laser settings.

We linked pore morphologies to energy input, with high line energy associated with approximately spherical keyhole defects. More irregular defects could be generated by using a very low hatch spacing, assumed to be due to powder denudation, or low energy, assumed to be lack of fusion.

When using manufacturer recommended settings, with small samples, we found it was possible to make small improvements (reductions) to the pore volume fraction by increasing the energy input. However, we also know that the geometry influences the number of pores so cannot be sure that this effect would be replicated across any given geometry. Furthermore, whether these small improvements are meaningful given the uncertainty outlined above remains to be seen. In addition, these small changes to the volume fraction need to be evaluated to understand whether they provide a useful change to the fatigue life of samples.

TASK6-10,12

Several melt strategies were selected for manufacturing fatigue specimens, representing differing levels of porosity. For samples subjected to the same post build heat treatment, the settings defined in this project outperformed manufacturer proposed settings.

When Basquins equation was fitted to samples made using a single melt strategy it was often able to adequately model the results. Attempts to combine data from different manufacturing strategies suggests that the pore size is less important than would be suggested by the stress intensity factor, and should be raised to $^1/_6$ rather than ½, when predicting fatigue life. The location of the pore on the other hand was a significant factor, with those at the surface associated with a shorter life. However, without more data it is difficult to draw numerical relationships.

When artificial defects were introduced into wrought and LPBF material, it corroborated our suggestion that pore size should be raised to $^{1}/_{6}$ in order to reduce the scatter in fatigue life model fitting. It was found that two defects in line with the stress behaved very similarly to a single defect, whereas when two pores were normal to the stress behaved worse than a single defect, but were not as detrimental as a defect of twice the size. When artificial defects were introduced into LPBF material it was found that LPBF outperformed wrought material subjected to the same stress intensity factor, but also showed more scatter. This implies that some of the scatter in LPBF fatigue life cannot be explained by consideration of the pores alone, and the local microstructure must be considered as well.

Our data suggests that increasing the energy density leads to more denser samples and greater fatigue life. We also suggest that removing the outer 0.5 mm of material from LPBF would remove an area that was found to be more porous with a range of melt strategies. However, the exact distribution of pores should be examined, to ensure any material removal does not bring a peak in porosity to the surface.

However, the very limited information about heat treatment we have suggests that this can have a more significant influence on the overall fatigue life than the laser manufacturing settings.

TASK11

A paper has been submitted covering the work in TASK1, several other papers are in work (see section 1.3).

4.1 Future work

Work is ongoing to identify the exact location in the CT data where the samples failed from. This currently is a manual process requiring alignment of SEM and CT data. The PhD student will continue work with these samples to extract more data. They will try to see if the critical characteristics of the defect that lead to failure can be identified. To increase our numerical data, stepped testing will be applied to those samples that reached runout. Once failed, we can add the pore data to our analysis. More detailed fracture surface analysis will be carried out to see if the pore morphology and local environment, i.e., other pores, can be linked to fatigue life.

The PhD student who was working on this project is currently writing their thesis and will be completing in 2024. They will also complete more desk studies of existing data to try and draw further conclusions.

The CT data regarding fatigue samples will be shared with University College Dublin, alongside information about the failure location, stress, and number of cycles to failure. Machine learning will be used to try to link the pore that caused failure to the life noted. UCD has experience working with machine learning for bending fatigue application, so will apply their techniques to uniaxial.

5. References

[1] "ASTM F2924-14, Standard Specification for Additive Manufacturing Titanium-6 Aluminum-4 Vanadium with Powder Bed Fusion, ASTM International, West Conshohocken, PA." ASTM International, 2014.

[2] "ASTM F2971-13, Standard Practice for Reporting Data for Test Specimens Prepared by Additive Manufacturing, ASTM International, West Conshohocken, PA,." 2013.

[3] "ASTM F3049-14, Standard Guide for Characterizing Properties of Metal Powders Used for Additive Manufacturing Processes, ASTM International, West Conshohocken, PA." 2014.

[4] K. Yakinthos, D. Missirlis, A. Palikaras, P. Storm, B. Simon, and A. Goulas, "Optimization of the design of recuperative heat exchangers in the exhaust nozzle of an aero engine," *Appl. Math. Model.*, vol. 31, no. 11, pp. 2524–2541, Nov. 2007, doi: 10.1016/j.apm.2006.10.008.

[5] H.-Y. Shih and Y.-C. Huang, "Thermal design and model analysis of the Swiss-roll recuperator for an innovative micro gas turbine," *Appl. Therm. Eng.*, vol. 29, no. 8, pp. 1493–1499, Jun. 2009, doi: 10.1016/j.applthermaleng.2008.06.029.

[6] B. Sundén, "7 - Heat exchangers and heat recovery processes in gas turbine systems," in *Modern Gas Turbine Systems*, P. Jansohn, Ed., in Woodhead Publishing Series in Energy. , Woodhead Publishing, 2013, pp. 224–246. doi: 10.1533/9780857096067.2.224.

[7] A. Traverso and A. F. Massardo, "Optimal design of compact recuperators for microturbine application," *Appl. Therm. Eng.*, vol. 25, no. 14, pp. 2054–2071, Oct. 2005, doi: 10.1016/j.applthermaleng.2005.01.015.

[8] A. Fatemi, R. Molaei, S. Sharifimehr, N. Phan, and N. Shamsaei, "Multiaxial fatigue behavior of wrought and additive manufactured Ti-6Al-4V including surface finish effect," *Int. J. Fatigue*, vol. 100, pp. 347–366, Jul. 2017, doi: 10.1016/j.ijfatigue.2017.03.044.

[9] H. Masuo *et al.*, "Effects of Defects, Surface Roughness and HIP on Fatigue Strength of Ti-6Al-4V manufactured by Additive Manufacturing," *Procedia Struct. Integr.*, vol. 7, pp. 19–26, Jan. 2017, doi: 10.1016/j.prostr.2017.11.055.

[10] "Engine Structural Integrity Program (ENSIP), MIL HDBK-1783B (USAF)." 2002.

[11] A. Vafadar, F. Guzzomi, A. Rassau, and K. Hayward, "Advances in Metal Additive Manufacturing: A Review of Common Processes, Industrial Applications, and Current Challenges," *Appl. Sci.*, vol. 11, no. 3, Art. no. 3, Jan. 2021, doi: 10.3390/app11031213.

[12] S. Tammas-Williams, "Correlating manufacturing strategies to material performance in Laser Powder Bed Fusion of Titanium 6Al-4V, Award number: FA9550-19-2-7001: Year 1 Performance Report." 2020.

[13] I. Jenkinson, "Correlating manufacturing strategies to material performance in Laser Powder Bed Fusion of Titanium 6Al-4V, Award number: FA9550-19-2-7001: Year 2 Performance Report." 2021.

[14] I. Jenkinson, "Correlating manufacturing strategies to material performance in Laser Powder Bed Fusion of Titanium 6Al-4V, Award number: FA9550-19-2-7001: Year 3 Performance Report." 2022.

[15] H. Gong, K. Rafi, H. Gu, T. Starr, and B. Stucker, "Analysis of defect generation in Ti–6Al–4V parts made using powder bed fusion additive manufacturing processes," *Addit. Manuf.*, vol. 1–4, pp. 87–98, Oct. 2014, doi: 10.1016/j.addma.2014.08.002.

[16] A. Soltani-Tehrani, M. Habibnejad-Korayem, S. Shao, M. Haghshenas, and N. Shamsaei, "Ti-6Al-4V powder characteristics in laser powder bed fusion: The effect on tensile and fatigue behavior," *Addit. Manuf.*, vol. 51, p. 102584, Mar. 2022, doi: 10.1016/j.addma.2021.102584.

[17] E. S. L. Gastal and M. M. Oliveira, "Adaptive manifolds for real-time high-dimensional filtering," *ACM Trans. Graph.*, vol. 31, no. 4, p. 33:1-33:13, Jul. 2012, doi: 10.1145/2185520.2185529.

[18] "Thermo Fisher Scientific, Avizo Software User's Guide." 2021.

[19] "SAE International, Heat Treatment of Titanium and Titanium Alloys, AMS-H-81200 REV. D." 2014.

[20] R. A. Brockman, A. L. Pilchak, W. John Porter, and R. John, "Estimation of grain boundary diffusivity in near-α titanium polycrystals," *Scr. Mater.*, vol. 65, no. 6, pp. 513–515, Sep. 2011, doi: 10.1016/j.scriptamat.2011.06.015.

[21] Y. Uematsu, T. Kakiuchi, Y. Han, and M. Nakajima, "Proposal of Fatigue Limit Design Curves for Additively Manufactured Ti-6Al-4V in a VHCF Regime Using Specimens with Artificial Defects," *Metals*, vol. 11, no. 6, Art. no. 6, Jun. 2021, doi: 10.3390/met11060964.

[22] "Holes," in *Peterson's Stress Concentration Factors*, John Wiley & Sons, Ltd, 2007, pp. 176–400. doi: 10.1002/9780470211106.ch4.

[23] S. Moon *et al.*, "Impact of surface and pore characteristics on fatigue life of laser powder bed fusion Ti–6Al–4V alloy described by neural network models," *Sci. Rep.*, vol. 11, no. 1, Art. no. 1, Oct. 2021, doi: 10.1038/s41598-021-99959-6.

[24] Y. Murakami, "Material defects as the basis of fatigue design," *Int. J. Fatigue*, vol. 41, pp. 2–10, Aug. 2012, doi: 10.1016/j.ijfatigue.2011.12.001.

[25] C. A. Schneider, W. S. Rasband, and K. W. Eliceiri, "NIH Image to ImageJ: 25 years of image analysis," *Nat. Methods*, vol. 9, no. 7, Art. no. 7, Jul. 2012, doi: 10.1038/nmeth.2089.

[26] S. Tammas-Williams, P. J. Withers, I. Todd, and P. B. Prangnell, "The Influence of Porosity on Fatigue Crack Initiation in Additively Manufactured Titanium Components," *Sci. Rep.*, vol. 7, no. 1, Art. no. 1, Aug. 2017, doi: 10.1038/s41598-017-06504-5.

[27] F. Bartolomeu, M. Gasik, F. S. Silva, and G. Miranda, "Mechanical Properties of Ti6Al4V Fabricated by Laser Powder Bed Fusion: A Review Focused on the Processing and Microstructural Parameters Influence on the Final Properties," *Metals*, vol. 12, no. 6, Art. no. 6, Jun. 2022, doi: 10.3390/met12060986.

[28] N. Otsu, "A Threshold Selection Method from Gray-Level Histograms," *IEEE Trans. Syst. Man Cybern.*, vol. 9, no. 1, pp. 62–66, Jan. 1979, doi: 10.1109/TSMC.1979.4310076.

[29] M. Thomas, G. J. Baxter, and I. Todd, "Normalised model-based processing diagrams for additive layer manufacture of engineering alloys," *Acta Mater.*, vol. 108, pp. 26–35, Apr. 2016, doi: 10.1016/j.actamat.2016.02.025.

[30] S.-H. Sun, K. Hagihara, T. Ishimoto, R. Suganuma, Y.-F. Xue, and T. Nakano, "Comparison of microstructure, crystallographic texture, and mechanical properties in Ti–15Mo–5Zr–3Al alloys fabricated via electron and laser beam powder bed fusion technologies," *Addit. Manuf.*, vol. 47, p. 102329, Nov. 2021, doi: 10.1016/j.addma.2021.102329.

[31] R. Snell *et al.*, "Methods for Rapid Pore Classification in Metal Additive Manufacturing," *JOM*, vol. 72, no. 1, pp. 101–109, Jan. 2020, doi: 10.1007/s11837-019-03761-9.

[32] A. Großmann, J. Felger, T. Frölich, J. Gosmann, and C. Mittelstedt, "Melt pool controlled laser powder bed fusion for customised low-density lattice structures," *Mater. Des.*, vol. 181, p. 108054, Nov. 2019, doi: 10.1016/j.matdes.2019.108054.

[33] Z. Gan *et al.*, "Universal scaling laws of keyhole stability and porosity in 3D printing of metals," *Nat. Commun.*, vol. 12, no. 1, Art. no. 1, Apr. 2021, doi: 10.1038/s41467-021-22704-0.

[34] Z. Wang and M. Liu, "Dimensionless analysis on selective laser melting to predict porosity and track morphology," *J. Mater. Process. Technol.*, vol. 273, p. 116238, Nov. 2019, doi: 10.1016/j.jmatprotec.2019.05.019.

[35] R. Cunningham *et al.*, "Keyhole threshold and morphology in laser melting revealed by ultrahigh-speed x-ray imaging," *Science*, vol. 363, no. 6429, pp. 849–852, Feb. 2019, doi: 10.1126/science.aav4687.

[36] P. Bidare, I. Bitharas, R. M. Ward, M. M. Attallah, and A. J. Moore, "Fluid and particle dynamics in laser powder bed fusion," *Acta Mater.*, vol. 142, pp. 107–120, Jan. 2018, doi: 10.1016/j.actamat.2017.09.051.

[37] S. Tammas-Williams, H. Zhao, F. Léonard, F. Derguti, I. Todd, and P. B. Prangnell, "XCT analysis of the influence of melt strategies on defect population in Ti–6Al–4V components manufactured by Selective Electron Beam Melting," *Mater. Charact.*, vol. 102, pp. 47–61, Apr. 2015, doi: 10.1016/j.matchar.2015.02.008.

[38] F. H. Kim, H. Yeung, and E. J. Garboczi, "Characterizing the effects of laser control in laser powder bed fusion on near-surface pore formation via combined analysis of in-situ melt pool monitoring and X-ray computed tomography☆," *Addit. Manuf.*, vol. 48, p. 102372, Dec. 2021, doi: 10.1016/j.addma.2021.102372.

6. List of Symbols, Abbreviations and Acronyms

6.1 Abbreviations and Acronyms

AFRL	Air force research laboratory
AM	Additive manufacture
CT	Computed tomography
LJMU	Liverpool John Moores University
LPBF	Laser powder bed fusion
PBF	Powder bed fusion
PSD	Particle size distribution
SIF	Stress intensity factor
UoE	The University of Edinburgh
UoL	The University of Liverpool
UoH	The University of Huddersfield
UoS	The University of Sheffield
VF	Volume fraction

6.2 Symbols

η	Absorptivity	-
A_n	Area of pore that caused failure	μm^2
T_m	Bed temperature	K
R^2	Coefficient of determination	-
K_f'	Constant defined, analogous to σ_f'	$MPa.mm^{1/2}$
c	Constant defined, analogous to b	-
C	Constant proposed to normalise stress	-
ρ	Density	kg/m^3
E	Energy density	J/mm^3
ϕ_{AB}	Equivalent diameter as built	mm
ϕ_{SR}	Equivalent diameter stress relieved	mm
σ_w	Estimated stress limit at 10^8 cycles	MPa
t	Exposure time	µs
N_f	Fatigue cycles to failure	-
σ_f'	Fatigue strength coefficient	MPa
b	Fatigue strength exponent	-
R	Fatigue testing stress ratio	-
h	Hatch spacing	mm
q	Laser power	W
v	Laser scan speed	mm/s
r_b	Laser spot radius	mm
L_m	Latent heat of melting	J/kg
l	Layer thickness	mm
L_e	Line energy	J/mm
T_m	Melting temperature	K
d_{melt}^*	Normalised distance	-
E_0^*	Normalised energy density	-
h_{melt}^*	Normalised hatch spacing	-

l_{melt}^{*}	Normalised layer thickness	-
q_{k}^{*}	Normalised power by conduction	-
d	Point distance between exposures	µm
C_p	Specific heat capacity	J/Kg/K
σ_a	Stress amplitude during fatigue testing	MPa
K_I	Stress intensity factor	MPa.mm$^{1/2}$
T_v	Vaporization temperature	K
HV	Vickers Hardness	HV

7. Appendix

Appendix A

Table 6: Measured porosity volume fraction again build parameters for a Renishaw system. Power, layer thickness and focus offset were held constant at 200 W, 30 µm and 0 mm, respectively.

Exposure time (µs)	Point Distance (µm)	Hatch spacing (µm)	Volume fraction (%)	Energy Density (J/mm^3)	Notes
50	**75**	**65**	**0.038**	**68.4**	***Standard settings*** **– used in user effect CT study**
50	75	65	0.026	68.4	*Unidirectional hatching*
50	75	65	0.022	68.4	*Contour then hatch*
50	75	65	0.012	68.4	*Double Contours*
60	75	65	0.005	82.1	
40	75	65	-	54.7	*Missing data*
50	90	65	0.083	57.0	
50	60	65	0.003	85.5	
50	75	78	-	57.0	*Missing data*
50	75	52	0.016	85.5	
60	90	65	0.075	68.4	
60	**60**	**65**	**0.009**	**102.6**	**High energy sample used in user effect CT study**
40	60	65	0.051	68.4	
40	**90**	**65**	**0.635**	**45.6**	**Low energy sample used in user effect CT study**
60	75	78	0.016	68.4	
60	75	52	0.035	102.6	
40	75	52	0.082	68.4	
40	75	78	0.008	45.6	
50	90	78	0.024	47.5	
50	90	52	0.018	71.2	
50	60	52	0.001	106.8	
50	60	78	0.015	71.2	
60	90	78	0.021	57.0	
60	60	78	0.018	85.5	
40	60	78	0.015	57.0	
40	60	52	0.030	85.5	
60	90	52	0.025	85.5	
60	60	52	0.008	128.2	
40	90	52	0.436	57.0	
40	90	78	0.214	38.0	

Appendix B

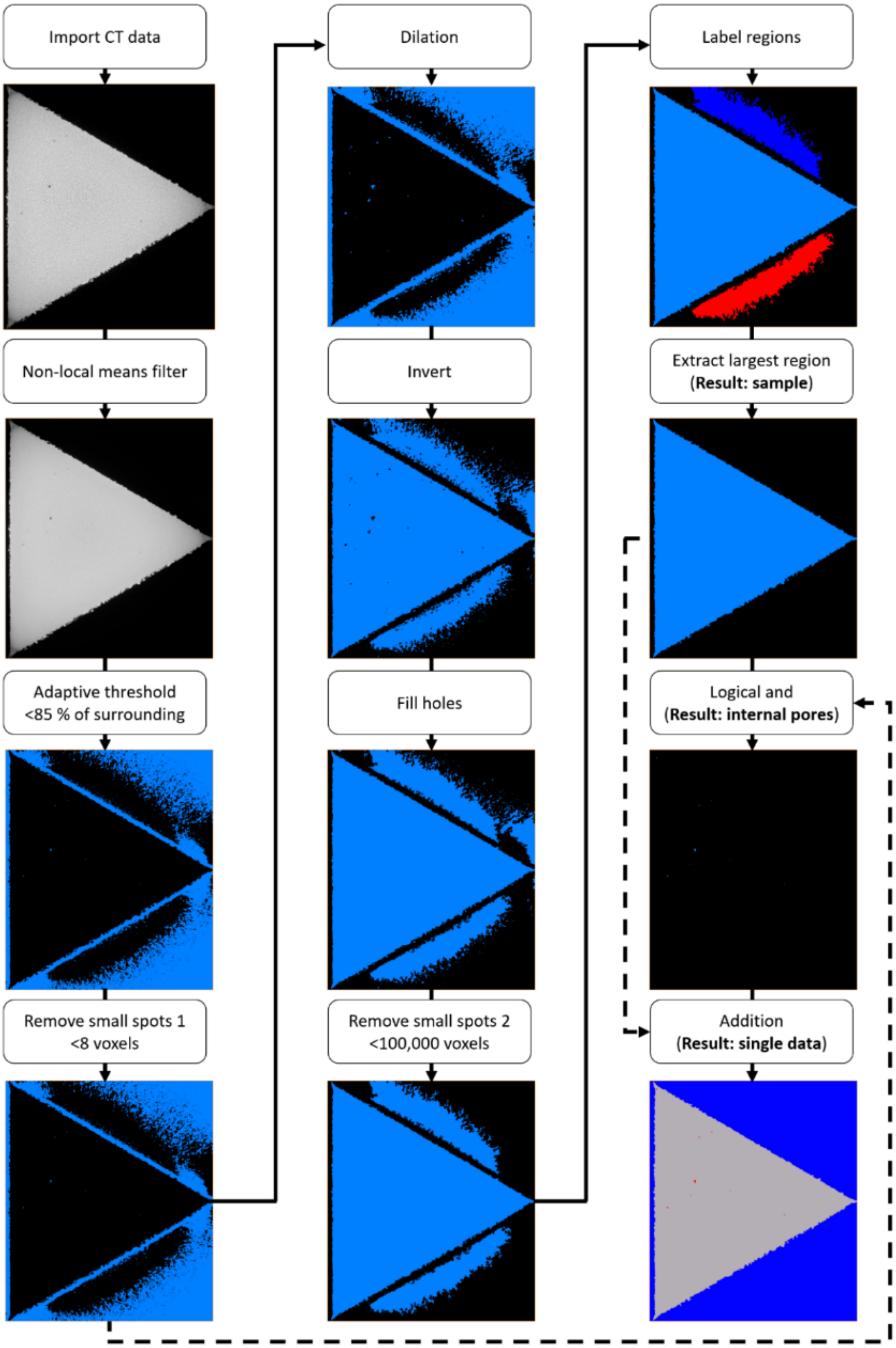

Figure 43: CT data workflow, showing example image processing. When an image is used twice, the initial use is indicated by the solid line while the secondary use by the dashed.